[American Journal of Science, Vol. 319, September, 2019, P. 549-581, DOI 10.2475/07.2019.02]

THE EFFECT OF SOIL TEMPERATURE SEASONALITY ON CLIMATE RECONSTRUCTIONS FROM PALEOSOLS

TIMOTHY M. GALLAGHER*,**,†, MICHAEL HREN***,
and NATHAN D. SHELDON*

ABSTRACT. Paleosols comprise an important archive of continental paleoclimate information throughout geologic history, but resolving temperature seasonality poses a challenge to the application of paleosol-derived temperature proxies. Not only does seasonality exert a strong control on the biosphere, but it can also obfuscate accurate interpretation of proxy records of paleotemperature. In order to examine the effect temperature seasonality has on paleosol temperature proxies, soil temperature data were compiled from over 200 stations that comprise the NRCS Soil Climate Analysis Network. Observed and modeled seasonal soil temperature variations were then compared to quantify system behavior. Greater than predicted soil temperature seasonality is observed at nearly half of the sites, driven primarily by direct heating of the soil surface by solar radiation. The ground-heating effect becomes more pronounced at sites receiving less than 600 mm of annual precipitation, with an average effect > 4 °C when mean annual precipitation falls below 300 mm. Large ground heating effects cannot be presumed for all carbonate-bearing paleosols, but the effect can be approximated when combined with paleo-precipitation estimates. Approximately two-fifths of sites record less temperature variation than predicted. This reduction in soil temperature seasonality is a result of warmer cold-season soil temperatures, driven by processes such as snow cover insulation and explains why pedotransfer functions break down below mean annual air temperatures (MAAT) of 6 to 8 °C. Clumped isotope measurements of pedogenic carbonate from a stacked series of late Eocene paleosols from Northeastern Spain are also examined to demonstrate how the documented seasonal trends in modern soils can inform paleo-applications, by considering carbonate formation depth and predicted ground heating effect. These paleosol results are best explained by a MAAT of ~27 °C with annual temperature seasonality of 25 °C.

Key words: clumped isotopes, thermal damping, ground heating, pedotransfer function, Eocene

INTRODUCTION

Accurate continental temperature reconstructions provide important constraints on climate sensitivity to changes in atmospheric pCO_2 (for example Steppuhn and others, 2007; Huber and Caballero, 2011), the timing and rates of tectonic uplift (for example Fan and others, 2014; Garzione and others, 2014), and the driving mechanisms and feedbacks associated with mass extinction events (for example McElwain and others, 1999; Retallack and others, 2003). When reconstructing temperatures, it is important to consider shifts in temperature seasonality alongside warming or cooling trends in mean annual air temperature (MAAT), because a single MAAT encompasses a wide range of ecosystems that represent a spectrum of temporal variations in precipitation and temperature on an annual cycle. Seasonal temperature variations also often exceed extreme warming or cooling trends in MAAT. For example, warming estimates range between 3 and 7 °C in the continental interior of North America during Paleocene-Eocene Thermal Maximum (Koch and others, 2003; Wing and

* Department of Earth and Environmental Sciences, University of Michigan, Ann Arbor, Michigan, 48109, USA
** Department of Geological Sciences, University of Texas at Austin, Austin, Texas, 78712, USA
*** Center for Integrative Geosciences, University of Connecticut, Storrs, Connecticut, 06269, USA
† Corresponding author: gallagher@jsg.utexas.edu

others, 2005). These warming estimates are relatively small when compared to the magnitude of seasonal temperature fluctuation observed in modern terrestrial settings, which can vary from < 5 °C on islands and coastal settings to > 40 °C in continental interiors (NCDC, 2012).

The need to investigate changes in continental seasonality is especially important at major climate transitions in the geologic past. These global events are typically revealed by fairly consistent trends in marine records, but the climate expression on land is often more heterogeneous. For example, the Eocene-Oligocene transition is generally understood to be a global cooling event evidenced by a positive shift in marine $\delta^{18}O$ records (Coxall and others, 2005; Pearson and others, 2008; Coxall and Wilson, 2011) linked to a decline in atmospheric CO_2 (Pearson and others, 2009) and the onset of Antarctic glaciation (for example Lear and others, 2008; Galeotti and others, 2016). While some continental temperature records show significant cooling at this time (for example Zanazzi and others, 2007; Hren and others, 2013; Fan and others, 2017; Colwyn and Hren, 2019), climate reconstructions from other regions appear relatively stable through the Eocene-Oligocene transition (Retallack, 2007; Sheldon and others, 2012; Kohn and others, 2015). Therefore, it is important to investigate if climate in these latter regions was truly stable, or if there were significant changes in climate seasonality not detected by traditional paleosol proxies.

Paleosols comprise an important archive of terrestrial paleoenvironmental data that may provide insight on changes in seasonality (Sheldon and Tabor, 2009; Tabor and Myers, 2015). Proxies developed for reconstructing temperature from paleosols include both "pedotransfer functions" and mineral-specific approaches. Pedotransfer functions relate the degree of chemical weathering, as recorded by the bulk elemental geochemistry of paleosols, to MAAT (Sheldon and others, 2002; Gallagher and Sheldon, 2013; Stinchcomb and others, 2016). Mineral-based temperature proxies use the stable isotopic geochemistry of minerals that form *in situ* in soils, such as carbonate (Dworkin and others, 2005; Ghosh and others, 2006b), clays (Delgado and Reyes, 1996; Sjostrom and others, 2004; Tabor and Montañez, 2005; Grujic and others, 2018), and iron (hydr)oxides (Yapp, 1987; Yapp, 2000; Sjostrom and others, 2006).

Within these mineral-based proxies, carbonate clumped isotope thermometry has emerged as a promising approach for reconstructing temperatures from paleosol carbonate. It is based on the observation that the abundance of doubly-substituted carbonate isotopologues (that is isotopologues containing at least two rare isotopes; for example, $^{13}C^{16}O_2^{18}O^{2-}$) varies as a function of temperature alone (Ghosh and others, 2006a). Clumped isotope geochemistry allows the formation temperature of paleosol carbonate to be assessed directly (for example, Quade and others, 2013; Snell and others, 2013; Kelson and others, 2018), because doubly-substituted isotopologues become increasingly abundant at lower calcite formation temperatures, well above what would be expected if the isotopes were randomly distributed throughout the crystal lattice (Eiler, 2011).

Determining clumped isotope temperatures of paleosol carbonate can provide constraints on warm season surface temperatures, because, pedogenic carbonate formation occurs during the warm-season in many modern soils (Breecker and others, 2009; Passey and others, 2010; Quade and others, 2013; Hough and others, 2014). These estimates of warm season temperatures can be combined with independent MAAT estimates to constrain the magnitude of temperature seasonality in the geologic past (Snell and others, 2013; Hyland and others, 2018). However, a warm-season formation temperature cannot always be assumed, because in certain settings regional hydrologic patterns can promote carbonate formation outside of the warm season (Peters and others, 2013; Gallagher and Sheldon, 2016).When interpreting geochemistry data from paleosol carbonate, it is important to consider that these data will be

reflective of the soil temperature at the time of formation rather than the surface air temperature.

Soil temperature variability at depth is ultimately controlled by the magnitude and frequency of temperature variation at the soil surface. Surface temperature variations are progressively damped and lagged with increasing soil depth because some heat is absorbed or released along the propagation path (Hillel, 1980). Diurnal surface temperature variations are typically damped out by 50 cm, whereas the effects of seasonal air temperature variation can be propagated many meters below the soil surface (Hillel, 1980). Additional factors can cause soil surface temperature to deviate from that of overlying air. For example, direct solar irradiation of the soil surface can cause soil temperatures to become significantly warmer than the overlying air temperatures (Geiger and others, 1995; Quade and others, 2013). Therefore, there is a need to identify the processes that cause soil temperatures to deviate systematically from air temperatures and quantify the effects these processes will have on paleosol proxies.

To address this need, we compiled seasonal temperature data from over 200 soils that formed under disparate climates ranging from tropical islands to continental interiors. We compare the soil temperature data to seasonal air temperature fluctuations in order to identify and quantify systematic differences between the observed magnitude of soil temperature seasonality and the value predicted by seasonal air temperature variation alone. Comparison of observational air and soil temperature data is used to assess the effects that seasonal temperature variations have on temperatures reconstructed from the geochemistry of paleosols. We then use these modern observations to evaluate new clumped isotope temperatures derived from paleosol carbonate nodules from the late Eocene of northeastern Spain.

METHODS

Modern Data Compilation

Modern soil temperature data were compiled from over 200 soil monitoring stations that comprise the Soil Climate Analysis Network (SCAN) (Schaefer and others, 2007; NRCS, 2016). The SCAN dataset includes 219 stations distributed across the contiguous United Sates, Alaska, Hawaii, Puerto Rico, and the U.S. Virgin Islands (Appendix fig. A1). Annual time series datasets consist of one temperature value recorded each day at midnight. At most SCAN sites, temperature sensors are installed at 5, 10, 20, 51, and 102 cm depth. Data was analyzed from 51 and 102 cm depth in order to avoid complications associated with diurnal temperature fluctuations, which are largely damped out by 50 cm (Hillel, 1980). These soil depths are also relevant for environmental reconstructions derived from the geochemistry of soil carbonate, because the $\delta^{13}C$ of soil CO_2 typically does not stabilize until 30 to 50 cm depth in the soil (Cerling, 1999). Average monthly soil temperature values were subsequently calculated by averaging all available daily temperature values corresponding to that month recorded between the station installation date and December 31, 2015. Not every SCAN site had sensors installed at both 51 and 102 cm, and sites were excluded if there was less than 1 complete year of temperature data at a particular depth. Adequate soil temperature data at 51 cm and 102 depth were available for 206 sites and 194 sites, respectively (Appendix table A1).

Monthly normal average air temperatures for each SCAN site are derived from the 1981–2010 U.S. climate normal dataset (Arguez and others, 2012). Because large elevation discrepancies exist between some SCAN sites and proximal climate stations, air temperature normals for SCAN sites within the contiguous United States were taken from the PRISM 800 m gridded dataset, which modeled temperatures using a digital elevation model as the predictor grid (PRISM Climate Group, 2015). The closest climate normal station of comparable elevation was used for the SCAN sites

outside of the contiguous United States, because the PRISM dataset does not cover Alaska, Hawaii, or the Caribbean. Twelve of these sites were excluded from further analysis because either the distance (> 20 km) or the elevation difference (> 125 m) between the SCAN sites and nearby climate stations was too large. The average distance between the remaining SCAN sites and climate stations was 6 km.

The predicted magnitude of soil temperature seasonality at depth was modeled as a function of depth (z) and time (t) using the following equation:

$$T(z,t) = T_{avg} + A_0 \frac{\sin\left(wt - \frac{z}{d}\right)}{e^{\frac{z}{d}}} \quad (1)$$

where, T_{avg} is the average soil temperature, A_0 is the amplitude of temperature variation at the soil surface, ω is the radial frequency, and d is the damping depth (Hillel, 1980). The damping depth varies according to texture and water content and can be calculated from the thermal conductivity (κ) and volumetric heat capacity (C_v) of the soil as follows:

$$d = \left(2 \times \frac{\frac{\kappa}{C_v}}{\omega}\right)^{\frac{1}{2}} \quad (2)$$

For the purposes of this study, the predicted soil temperature seasonality at depth was modeled by assuming that variations in soil surface temperatures were driven only by air temperature fluctuations. T_{avg} was assumed to equal MAAT and A_0 was calculated using the maximum and minimum average monthly air temperatures. The damping depth was calculated using average values of κ (1.02 W/m/°K) and C_v (2.08 J/m^3/°K) that were empirically determined for six different soil textures over a range of eight different water contents (Shukla, 2014). This approach predicts that at 51 and 102 cm depth soil temperature seasonality will be reduced, respectively, to 80% (n = 45; StDev = 2.8%) and 63% (n = 45; StDev = 4.4 %) of air temperature seasonality. Figure 1 shows the modeled soil temperature results for the Rogers Farm #1 SCAN site as an example. This simplified modeling approach allows for the identification of systematic deviations between soil and surface air temperatures that exist across a wide variety of soil types and environment. Identification of these systematic deviations is important for paleosol-derived environmental reconstructions, because presently it is not possible to reconstruct factors known to affect soil temperature such as snowpack and vegetative shade.

Paleosol Temperature Reconstruction

Paleosol carbonate nodules analyzed as part of this study were collected from the Maians-Rubio composite section of the Artés Formation and were described in Sheldon and others (2012). This original age model for this section spanned the Eocene-Oligocene boundary in the Ebro Basin, NE Spain (Costa and others, 2011); however the paleosol bearing interval has since been revised to be late Eocene (Garcés and others, 2018). Carbonate nodules from 10 of the paleosols were analyzed for carbonate clumped isotope composition following the methods described in Defliese and others (2015). In brief, 5 to 10 mg of drilled sample was reacted in anhydrous phosphoric acid held at 75 °C. The resulting CO_2 was purified off-line via cryogenic separation and a column filled with Porapak-Q resin held at −25 °C. The samples, carbonate standards, gas standards equilibrated with H_2O at 25 °C, and gas standards heated to 1000 °C were then analyzed on a Thermo MAT 253 dual-inlet mass

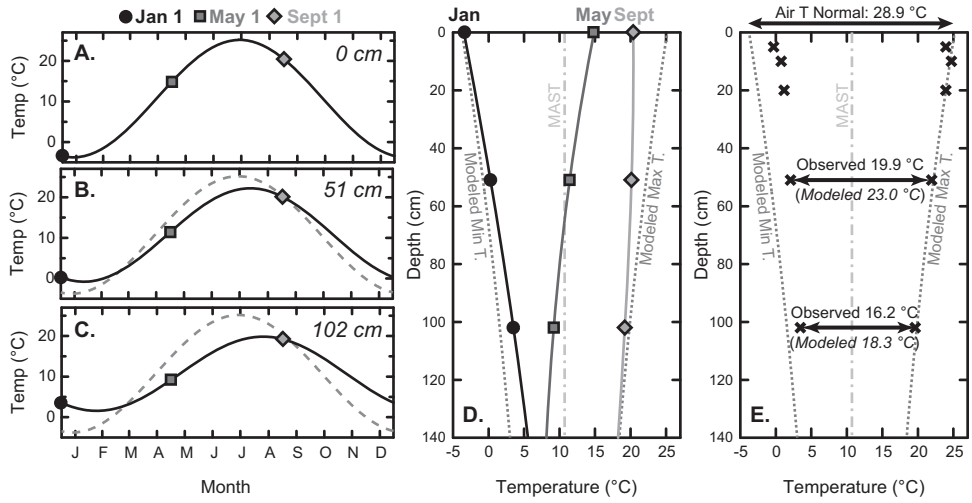

Fig. 1. Example of modeled soil temperature at the Rogers Farm #1 SCAN site (Site # 2001). Modeled soil temperature variation throughout the year at (A) 0 cm, (B) 51 cm, and (C) 102 cm. The dashed gray line (B–C) corresponds to the temperature at 0 cm. (D–E) Modeled soil temperatures vs. depth, where the dotted gray lines represent the absolute minimum and maximum temperature attained at a particular depth, and the dot-dashed gray line represents mean annual soil temperature (MAST). Black circles represent modeled soil temperatures on January 1st, dark gray squares represent May 1st, and gray diamonds represent September 1st. Black X's mark the observed warmest and coldest average monthly temperatures at instrumented soil depths. At this site, the observed temperature seasonality at 51 and 102 cm (19.9 and 16.2 °C) is less than the values predicted by the model (23.0 and 18.3 °C).

spectrometer at the University of Michigan Stable Isotope Laboratory. Carbonate clumped isotope data is reported in Δ_{47} notation and presented in the absolute reference frame of Dennis and others (2011). Simultaneously measured $\delta^{18}O$ and $\delta^{13}C$ values were corrected for fractionation in the Porapak column following Petersen and others (2016).

Δ_{47} values were converted to temperatures using the empirical calibration of Kluge and others (2015) This calibration was selected because it includes samples formed across a wide range of temperatures (25–250 °C), and it is statistically similar to an independent calibration developed within the University of Michigan Stable Isotope Lab (Defliese and others, 2015). Some uncertainty persists around the choice of clumped isotope temperature calibration due to observed discrepancies between empirical calibrations developed at different laboratories. Recent studies have observed that the choice of ^{17}O correction factors may sit at the source of uncertainty (Daëron and others, 2016; Schauer and others, 2016). Reprocessed data using Brand and others (2010) coefficients are included in Appendix tables A2 and A3; however, in the absence of a calibration at the UM Stable Isotope Laboratory that incorporates those parameters, we will only discuss temperatures calculated using the original approach.

RESULTS

Modern Soil Data

Soil and air temperature seasonality data are plotted against one another in figure 2 and summarized in Appendix table A1. The observed magnitude of soil temperature seasonality at 51 and 102 cm ranges between 1 to 31 °C and 1 to 25 °C, respectively. The absolute range of air temperature seasonality at the SCAN sites is slightly larger, varying

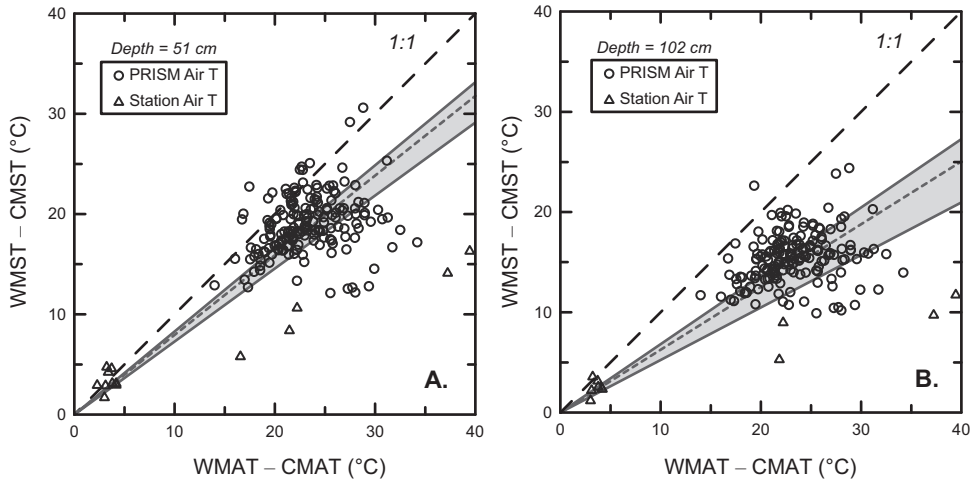

Fig. 2. Soil temperature seasonality vs. air temperature seasonality at (A) 51 and (B) 102 cm depth. The black, wide-dashed lines are 1:1 lines. Gray regions illustrate the absolute range of predicted soil temperature seasonality values based on air temperature fluctuations and empirically-derived soil thermal properties from Shukla (2014). The upper and lower bounds of this region are calculated with thermal conductivity and volumetric heat capacity values that predict the smallest and largest temperature damping effects, respectively. The gray dashed line (the slope is 0.80 at 51 cm depth and 0.63 at 102 cm depth) is the predicted soil temperature seasonality calculated using average thermal conductivity and volumetric heat capacity values. WMAT – warm month mean air temperature, CMAT – cold month mean air temperature, WMST – warm month mean soil temperature, CMST – cold month mean soil temperature.

from 2 °C on Hawai'i to 39 °C in the Alaskan Interior. As expected, the observed temperature seasonality is progressively reduced deeper into the soil. At 51 cm depth in the soil, the observed soil temperature seasonality is less than air temperature seasonality at the majority of sites (88%). By 102 cm depth, the soil temperature seasonality exceeds that of the air at only two sites.

The magnitude of observed soil temperature variation strongly deviates from predicted values that assume seasonal air temperature and soil textural differences are the only drivers of soil temperature variation. A predictive window of soil temperatures was constructed using the C_v and κ values that produce the absolute minimum and maximum amounts of temperature damping in the soil (Shukla, 2014), shown as the gray shaded area in figure 2. The observed soil temperature seasonality does not fall within the predictive window at over half of the sites. At 51 cm depth, only 29 percent of the sites fall within the predicted range. Nearly half (49%) of the sites record a greater temperature seasonality than predicted, whereas two-fifths (22%) record less temperature seasonality than predicted. Data from 102 cm has a similar pattern, although slightly more of the sites fall within the predictive range (42%). 44 percent of the sites record greater seasonality than predicted, and 14 percent record less than predicted.

Paleosol Data

The Δ_{47} values of pedogenic carbonate range between 0.613 and 0.694 permil, with all but one sample having values greater than 0.652 permil (table 1). Complete clumped isotope results are presented in Appendix tables A4 and A5. Long-term measured values for the Carrara marble standard average 0.418 permil with a standard deviation of 0.020 permil. The latter value was used when calculating standard errors for samples with a standard deviation of replicate analyses less than that of the

TABLE 1

Paleosol carbonate geochemistry results

Sample	Section Height (m)	Age (Ma)[a]	n[b]	$\delta^{13}C$ (‰) VPDB	$\delta^{18}O$ (‰) VPDB	Δ_{47}(‰) ARF[c]	σ (‰)[d]	± 1 S.E. (‰)[e]	Temp (°C) 'Kluge'[f]	± 1 S.E. (°C)
MC-20	342.5	35.10	3	-0.8	-1.6	0.613	0.016	0.012	58	5
MC-19	329.2	35.12	3	-4.3	-5.9	0.669	0.010	0.012	35	4
MC-18	305.7	35.17	3	-5.0	-6.3	0.694	0.019	0.012	26	4
MC-17	293.5	35.19	5	-4.3	-4.9	0.655	0.021	0.009	41	4
MC-16	272.5	35.23	4	-5.0	-5.3	0.690	0.016	0.010	28	4
MC-15	259.2	35.25	4	-5.3	-5.9	0.690	0.021	0.010	28	4
MC-14	253.0	35.26	4	-4.9	-5.9	0.680	0.010	0.010	31	4
MC-13	243.2	35.28	3	-4.5	-4.9	0.652	0.016	0.012	42	5
MC-11	207.7	35.35	4	-5.4	-5.3	0.662	0.023	0.011	38	4
MC-9	180.5	35.39	3	-4.7	-5.9	0.675	0.006	0.012	33	4

[a] Age model from Sheldon and others (2012).
[b] Number of replicate analyses.
[c] Values normalized to the absolute reference frame (ARF) of Dennis and others (2011).
[d] Standard deviation of replicate analyses.
[e] Standard error calculated by dividing σ by the square root of n, where σ is calculated from replicate analyses unless it is exceeded by the long-term σ of standards (0.020 ‰).
[f] Temperature calibration of Kluge and others (2015).

long-term Carrara standard. This corresponds to a temperature range of 26 to 58 °C, with only one sample exceeding 42 °C (table 1). $\delta^{18}O$ values of paleosol carbonate samples range from −6.3 to −1.6 permil, and the $\delta^{13}C$ values range between −0.8 and −5.4 permil.

DISCUSSION

In order to quantify systematic deviations of soil temperature seasonality from air temperature seasonality, the magnitude of observed seasonal soil temperature variation can be compared to a predicted value that is modeled using seasonal air temperature fluctuations alone. Greater than predicted soil temperature seasonality occurs at 49 percent of sites and is best explained by direct heating of the soil surface by solar radiation. In contrast, the 22 percent of sites at which the predicted soil temperature seasonality is less than predicted can best be explained by cold-season phenomena, such as snow insulation. The physical processes driving the expansion and reduction of soil temperature seasonality relative to air temperature are discussed below, alongside their implications for paleosol based climate reconstructions.

Ground Heating and Soil Temperature Seasonality Expansion

The expansion in soil temperature seasonality observed at approximately half of the SCAN sites (fig. 2) is largely driven by warmer than predicted summer soil temperatures. In certain settings, soil surface temperatures can exceed the overlying air temperature due to absorption of solar radiation at the soil surface. For example, maximum soil surface temperatures in excess of 60 °C have been measured in desert environments (Geiger and others, 1995). These daily extreme temperatures are restricted to the upper portion of the soil, because diurnal temperature variation is largely damped out by 50 cm depth in the soil (Hillel, 1980). However, the effect of solar ground heating will be propagated deep into the soil if daily mean soil surface temperatures are also elevated above that of the air.

To explore the factors underlying the expansion in soil temperature seasonality, observed warm month mean soil temperatures (WMST) at a particular soil depth are compared to an equivalent value predicted by the simple soil temperature model. The maximum "daily" temperature predicted by the model is considered the most

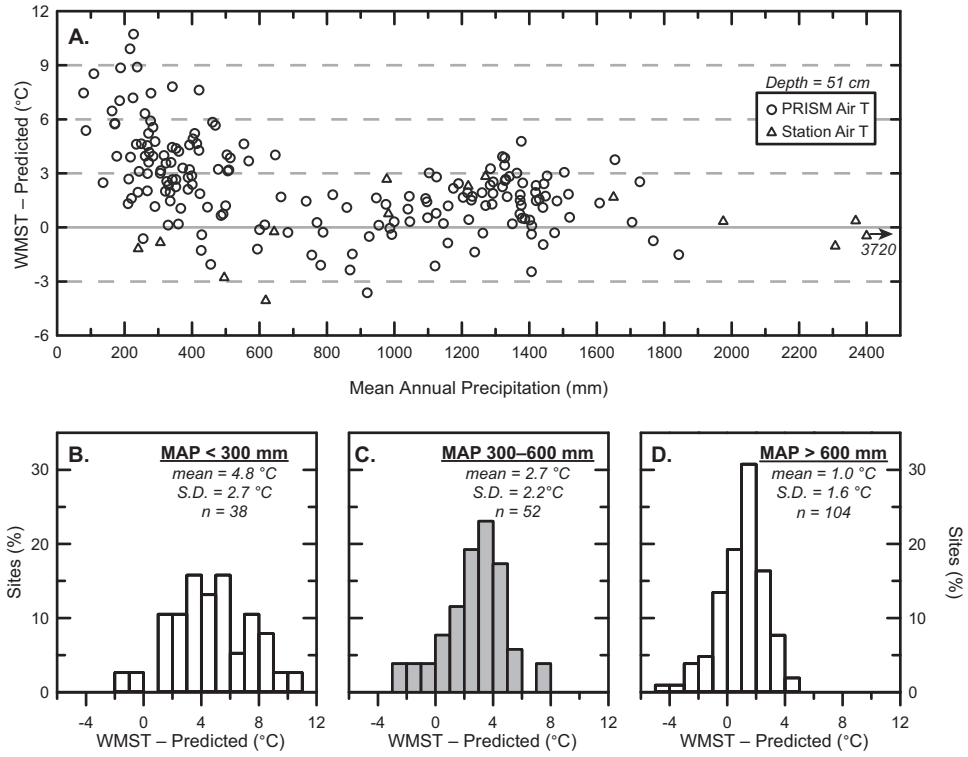

Fig. 3. (A) Mean annual precipitation (MAP) values vs. the difference between the observed warm month mean soil temperature (WMST) at 51 cm depth and the maximum temperature predicted based on air temperature fluctuations alone. Distributions of the difference between the observed and predicted maximum monthly average soil temperature values at (B) sites with MAP below 300 mm, (C) sites with MAP values between 300–600 mm, and (D) sites with MAP > 600 mm.

appropriate comparison to observed WMST values, because the model was forced using monthly average air temperatures, not daily values. Considering all of the sites together, the observed WMST exceeds the model predicted value by an average of 2 °C at both 51 and 102 cm.

A pattern emerges when differences between the observed and predicted WMSTs are compared to MAP values (figs. 3 and 4). No clear relationship exists between these variables at sites that receive more than ~600 mm of annual precipitation, and the average difference between observed and predicted WMST values is 1.2 °C at sites with MAP > 600 mm (fig. 3). However, the effect of ground heating progressively becomes more pronounced at drier sites below this ~600 mm threshold. At 51 cm, the observed WMST exceeds the predicted value by an average of 4.8 °C at sites with MAP < 300 mm; whereas the difference is only 2.7 °C where MAP is between 300 to 600 mm (fig. 3). Similar patterns are observed at 102 cm soil depth (fig. 4).

Warm season soil temperatures are related to precipitation, because water availability modifies the thermal properties of the soil and affects the composition and density of overlying vegetation. Wet soils have a higher specific heat capacity than dry soils, and therefore, more energy will be required to warm a soil with high water content (Hillel, 1980). Evaporation of soil water will also have a net cooling effect on the soil (Hillel, 1980).

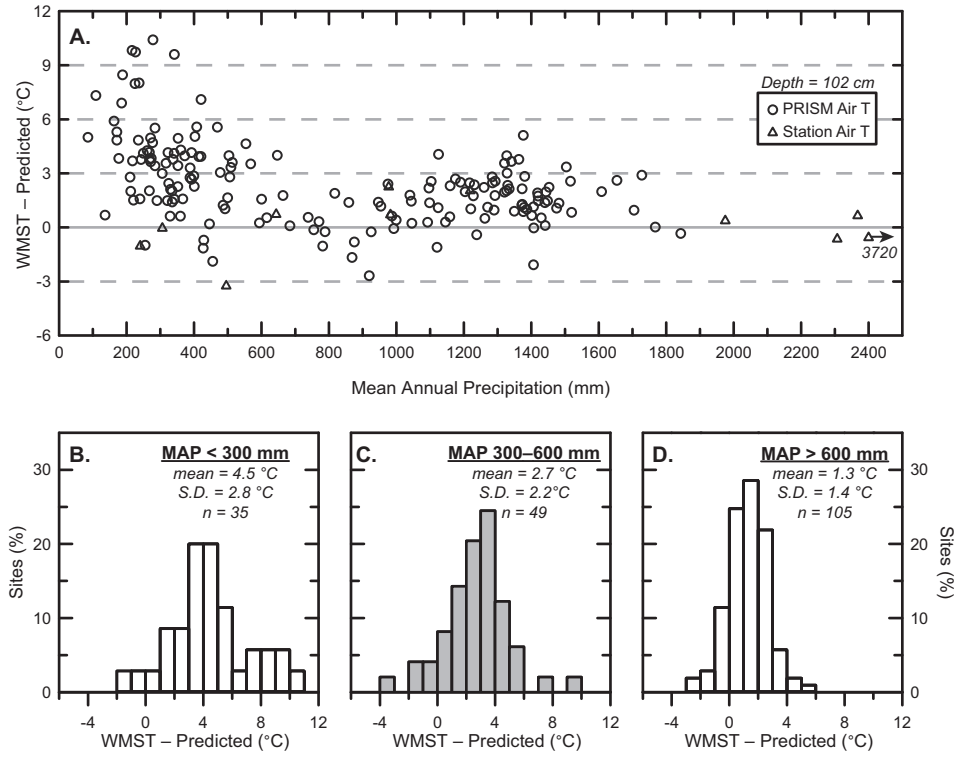

Fig. 4. (A) Mean annual precipitation (MAP) values vs. the difference between the observed warm month mean soil temperature (WMST) at 102 cm depth and the maximum temperature predicted based on air temperature fluctuations alone. Distributions of the difference between the observed and predicted maximum monthly average soil temperature values at (B) sites with MAP below 300 mm, (C) sites with MAP values between 300–600 mm, and (D) sites with MAP > 600 mm.

Warm season soil temperatures can also be enhanced in arid regions due to a decrease in vegetative cover. Vegetation affects soil thermal regimes by reducing the amount of solar radiation that reaches the ground and by modifying soil moisture distributions (Qashu and Zinke, 1964; Geiger and others, 1995). Vegetated soils experience less seasonal temperature variation than bare soils, and the type and density of vegetation will also have an effect. For example, summer soil temperatures measured at a site in Norfolk, England became progressively warmer and more variable within soils underlying dense forest, light forest, and grass (Oliver and others, 1987). Large differences in soil thermal regimes can also exist on a local scale within semi-arid savannas, with much cooler temperatures found under patches of canopy (Breshears and others, 1998). Replacement of native forest vegetation with crops or pasture potentially explains why some humid SCAN sites exhibit a larger ground heating effect than would otherwise be expected.

Higher than predicted soil temperatures complicate paleoclimate studies that aim to reconstruct air temperature from paleosols. Ground heating by solar radiation has been shown to affect the formation temperature and the geochemistry of pedogenic carbonate in modern soils. In a study of soils from the southwestern United States, India, and Tibet, Quade and others (2013) observed that the majority of pedogenic carbonate samples record clumped isotope temperatures elevated above warm season temperatures. Assuming that the carbonate formed at the hottest point of the year, an

additional 6 to 8 °C of surface heating would be required to account for the temperatures recorded at depth. In another clumped isotope study of modern pedogenic carbonate, Hough and others (2014) also observed that samples from Wyoming and Nebraska exceed warm season temperatures by 3 to 5 °C.

The relationship between MAP and the magnitude of ground heating can guide interpretations of paleosol geochemical data, especially if estimates of MAP independent from soil carbonate are available from bulk paleosol geochemistry (for example Sheldon and others, 2002; Nordt and Driese, 2010; Stinchcomb and others, 2016) or paleobotany (for example Picer and others, 2009; Peppe and others, 2011). Figures 3 and 4 illustrate that ground heating effects systematically increase once MAP values fall below 600 mm. Pedogenic carbonate can form in settings with MAP values in excess of 1000 mm under climates with large precipitation seasonality (Royer, 1999; Nordt and others, 2006); therefore, a large ground heating effect should not be presumed for all paleosols bearing pedogenic carbonate.

The seasonal timing of precipitation may also moderate the magnitude of ground heating. For example, a site that is water-limited during the summer when insolation is higher may experience more ground heating than a site that receives abundant rainfall during the warm season. When all sites are considered, only a weak relationship exists between the amount of precipitation received during the cold half of the year and the difference between observed and predicted WMST values (Appendix fig. A2). However, ten out of the eleven sites with the most extreme ground heating ($WMST_{observed–predicted} > 7$ °C) receive over 60 percent of their precipitation during the cold half of the year, suggesting that precipitation seasonality may amplify the ground heating effect in certain settings. Quade and others (2013) noted that all of their sites were characterized by strong seasonal precipitation, possibly explaining why the ground heating effect at their sites was consistently at the upper end values observed at the SCAN sites.

Reduction in Soil Temperature Seasonality

The smaller than predicted soil temperature seasonality observed at a quarter of SCAN sites is best explained by cold-season processes. Moderately strong linear relationships ($r^2 = 0.63$; 0.59) exist between the cold month mean air temperature (CMAT) and the difference between the observed and predicted soil temperature range at both 51 and 102 cm depth (figs. 5A and 5B), with colder CMAT values corresponding to a greater reduction in observed soil temperature seasonality relative to predicted values. The slope of the linear regression between CMAT and the difference between observed and predicted soil temperature seasonality becomes shallower at 102 cm, because of progressive damping with depth of the surface temperature variation. This relationship only holds for sites where the CMAT is below 0 °C. No relationship is observed at sites where cold month air temperatures remain above freezing (fig. 5).

The physical mechanism driving the reduction soil temperature seasonality at these cold-weather sites is likely a combination of snow cover and latent heat processes in the soil. Snow cover can result in both warming and cooling of underlying soils, with the net effect and the magnitude depending on the seasonal timing of snowfall and snowmelt, the thickness and structure of the snow cover, and the geographic location (Zhang, 2005). For example, as solar insolation increases during early spring, net cooling of soils can occur due to the high albedo and thermal emissivity of fresh snowfall. In contrast, snowfall during the late fall can lead to net warming of soils due to its low thermal conductivity and ability to insulate the soil surface from colder winter air temperatures. Latent heat processes can also reduce temperature seasonality at depth in a soil, because propagation of heat will slow when soils are in a freeze-thaw temperature range (Fuchs and others, 1978).

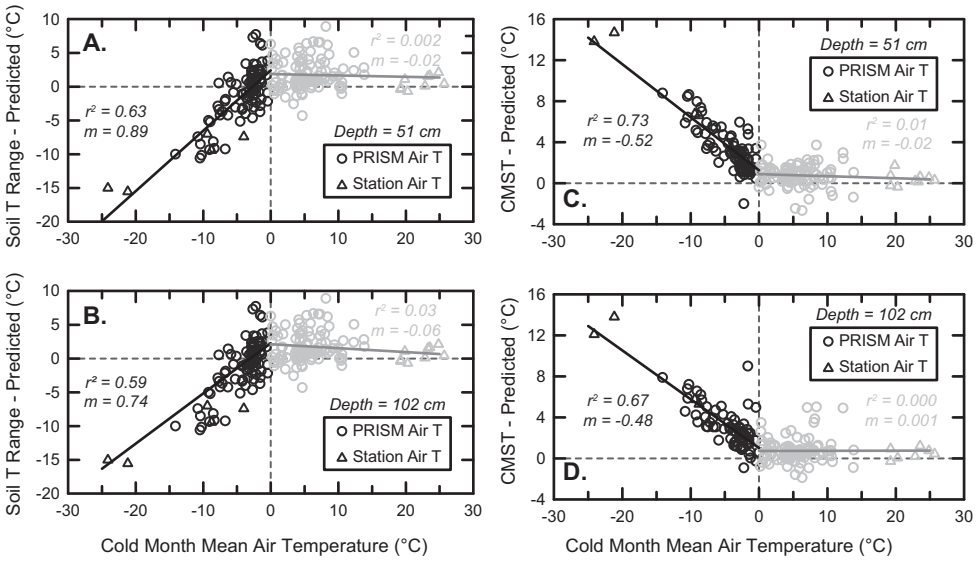

Fig. 5. Coldest month mean air temperature versus the difference between the observed soil temperature range at (A) 51 and (B) 102 cm depth and the range predicted based on air temperature fluctuations alone. (C–D) Coldest month mean air temperature versus the difference between the observed and predicted cold month mean soil temperature (CMST) based on air temperature fluctuations alone. T – temperature.

A stronger relationship is exhibited between CMAT and the difference between observed and predicted cold month mean soil temperature (figs. 5C and 5D). This relationship demonstrates that the smaller than predicted seasonality is being primarily driven by soil temperatures remaining warmer than predicted during the winter months, with insulation from snow cover playing an important role. Snow removal experiments documented that soil temperatures remained significantly warmer and exhibited less temperature variability in control plots where snow cover remained (Hardy and others, 2001; Decker and others, 2003).

Although sites with colder CMAT values record larger deviations in cold month soil temperature, the amount and seasonal timing of snowfall is not directly controlled by air temperature. For example, snowfall that occurs early in the season would be able to persist longer at the colder sites and produce larger soil temperature deviations. Differences in the timing and amount of snowfall likely account for the scatter in the relationship between CMAT and soil temperature. For example, the largest residual values from the regression line are from the Doe Ridge site in California (SCAN site #2191; Appendix table A1). This site is located in the Sierra Nevada and typically experiences high levels of snowfall and deep snow cover throughout the winter. Consistent snow cover throughout the winter months despite relatively mild temperatures (CMAT = −2 °) could explain the warmer than expected soil temperatures.

The smaller than predicted soil temperature seasonality at colder sites explains a consistent problem observed with pedotransfer functions, which struggle to predict colder MAAT values accurately. Sheldon and others (2002) identified a modest relationship between MAAT and the depletion of Na and K relative to Al, but the quality of this fit degrades towards lower temperatures as the scatter in the data increases. The PWI paleothermometer relates the base cation depletion to MAAT, but is incapable of estimating MAAT values below 9 °C (Gallagher and Sheldon, 2013). The $PPM_{1.0}$ model, which was developed using a much larger modern soil geochemis-

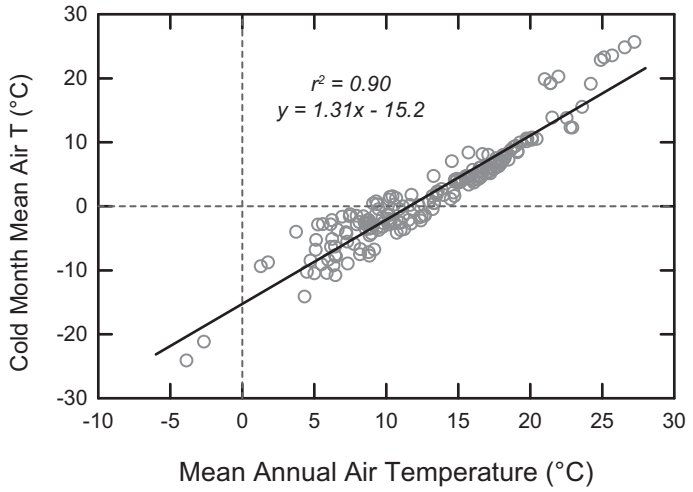

Fig. 6. Mean annual air temperature vs. cold month mean air temperature at SCAN sites analyzed as part of this study. T – temperature.

try dataset, systematically overestimates temperatures for soils that form where the observed MAAT is below ~6 °C (Stinchcomb and others, 2016).

Although these pedotransfer functions differ in their specific methodology, they are all based on the assumption that soils formed under warmer climates will undergo more chemical weathering and be more depleted in base cations. Conversely at lower air temperatures, weathering rates and cation leaching should be reduced. As described above, cold season soil temperatures begin to deviate significantly from the overlying air temperature once CMAT values fall below freezing. Beyond this threshold, the soil environment loses its direct relationship to air temperature. Higher soil temperatures than predicted during the winter will also increase the difference between mean annual soil temperatures (MAST) and MAAT (Smith and others, 1964). Increasing soil temperature could explain why soils formed below 6 °C are more weathered than expected and why the pedotransfer functions break down below this threshold. Colder MAAT values correspond to colder CMAT values, and it is not until MAAT values fall below ~6 to 8 °C that CMAT values consistently fall below 0 °C at all of the SCAN sites examined as part of this study (fig. 6). The pedotransfer functions were derived from soils sampled across a similar geographic distribution to the SCAN sites, so the relationship between MAAT and CMAT can be assumed to be similar.

With both the PWI and $PPM_{1.0}$, soils formed at sites with MAAT $<$ 6 °C appear to be more weathered than expected. Continued chemical weathering at near-zero soil temperatures is unsurprising as microbial communities remain active in soils insulated by snowpack (Sommerfeld and others, 1993; Brooks and others, 1997). Snowpack has also been shown to increase soil CO_2 concentrations by reducing diffusion out of the soil, potentially enhancing weathering (Solomon and Cerling, 1987). Furthermore, increased concentrations of Na in soil water during induced freeze-thaw events in snow removal experiments suggested freeze-thaw processes could also enhance soil weathering rates (Hentschel and others, 2009).

The disconnect between air and soil temperatures in cold settings combined with the potential enhancement of weathering at or near the freeze-thaw zone implies that MAAT values ~6 °C should be treated as a lower bound for the effectiveness of existing pedotransfer functions, unless specifically developed for cooler regions (for example

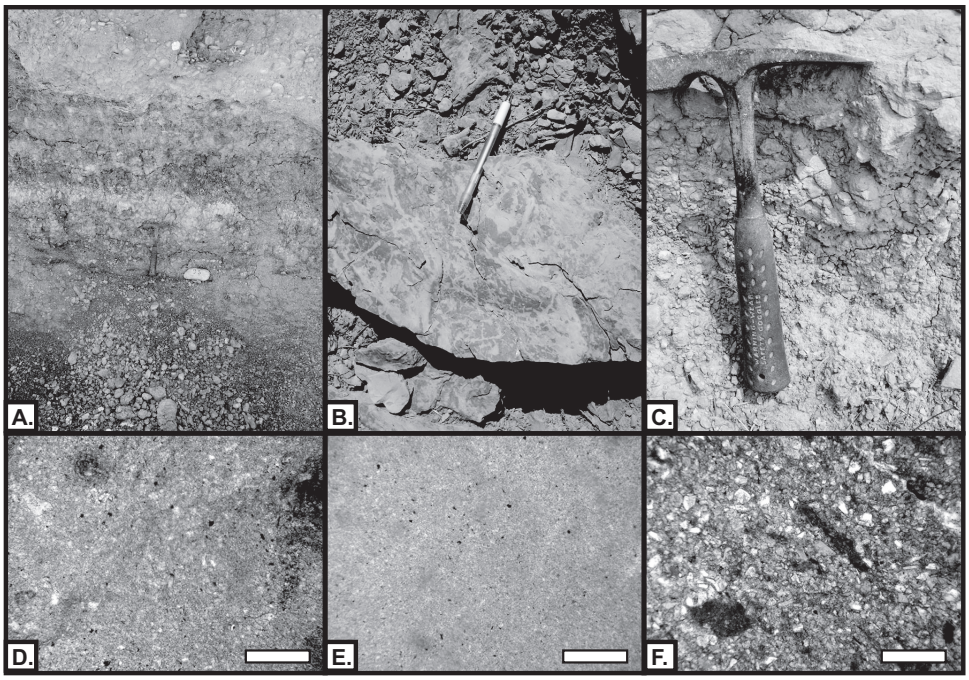

Fig. 7. (A–C) Outcrop images of paleosols and features from the Maians-Rubio section. (A) Well-developed Alfisol with Bk horizon just above the hammer. (B) Drab-haloed root traces. (C) Sub-vertical burrows in the upper part of the paleosol. Thin section images of carbonate nodule samples MC-9 (D), MC-14, and (F) MC-20. Scale bars are 10 μm.

Óskarsson and others, 2012). Caution should also be taken when applying pedotransfer functions if there is any independent evidence (textural features, pollen, *et cetera*) for average winter temperatures falling below 0 °C. Macromorphological paleosol features indicative of freezing conditions may include cryoturbation features and ice wedge casts (Van Vliet-Lanoë, 1998; Sanborn and others, 2006), whereas micromorphological features could include silt caps and granular fabrics (Van Vliet-Lanoë and others, 1984; Van Vliet-Lanoë and others, 2004).

Shifts in soil temperature seasonality driven by cold season processes are not expected to have an effect on temperatures recorded by soil carbonate that forms during the warm season, because these processes will generally not affect the maximum summer soil temperatures. Temperatures recorded by soil carbonate may be moderately affected at localities where carbonate formation occurs during the spring or fall and winter temperatures fall below 0 °C. This potential effect is because winter soil temperatures that remain warmer than the overlying air will cause MAST to shift to values warmer than MAAT.

Late Eocene Paleosols

The systematic deviations between soil temperature and air temperature described above can assist interpretations of paleosol geochemistry data, especially when evaluating possible changes in temperature seasonality. This insight can be applied to carbonate bearing paleosols from the late Eocene at the Maians-Rubio section in northern Spain. In general, paleosols are well-developed Inceptisols to weakly-developed Alfisols (fig. 7A). Paleosols contain abundant drab-haloed root traces (fig. 7B), rare calcareous

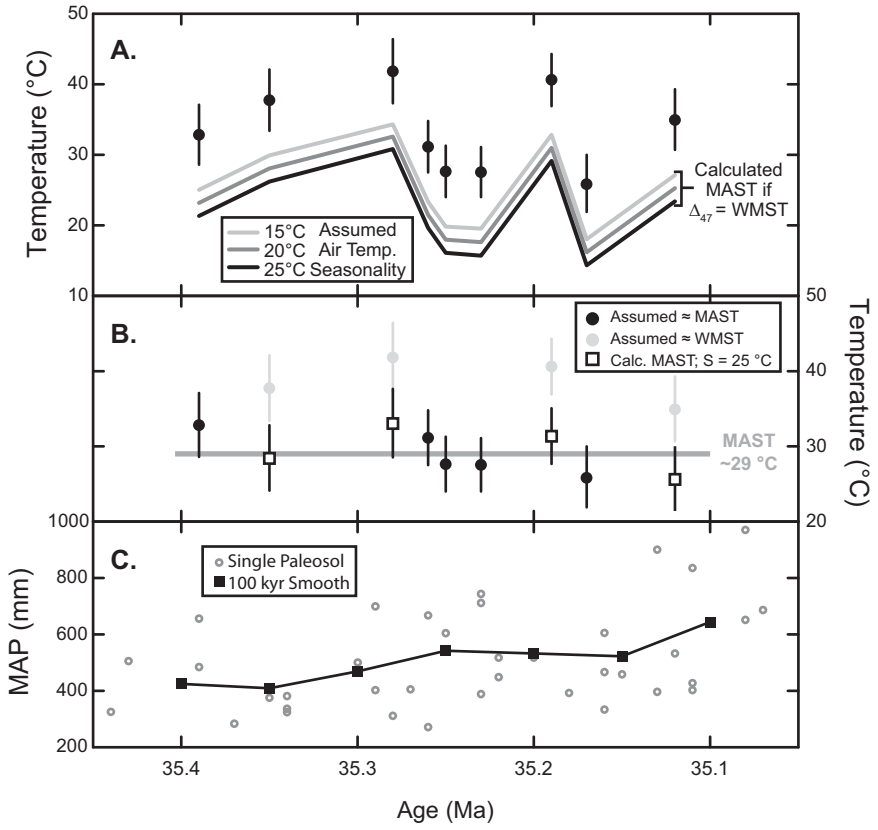

Fig. 8. (A) Black circles correspond to measured clumped isotope values (± 1 S.E.). Gray lines are the minimum allowable mean annual soil temperature (MAST) for three different air temperature seasonalities (15, 20, and 25 °C), assuming that the clumped isotope temperature accurately records warm month mean soil temperature (WMST). (B) To calculate the MAST and air temperature seasonality required to explain the range in clumped isotope temperatures in the absence of any change in MAAT during the late Eocene, samples within ± 1 S.E. of the coldest sample (MC-18) are assumed to equal MAST (black circles), while gray circles are assumed to approximate WMST. Horizontal gray bar is the average of MAST samples (29 °C). White squares represent the calculated MAST for the gray circles, assuming a temperature seasonality of 25 °C. (C) MAP estimates using the $PPM_{1.0}$ model of Stinchcomb and others (2016) using the bulk geochemistry data in Sheldon and others (2012). Black squares are a 100 kyr smooth with a 50 kyr step.

rhizoliths, and both calcareous and non-calcareous vertical to sub-vertical burrows preserved in the A or upper Bk horizon (fig. 7C). Grain size is typical silt-sized with few observed changes (fine sand to clay) independent of soil horizon. There is no evidence of preserved organic matter, with the exception of trace amounts occluded within carbonate nodules.

Previous investigation at the Maians-Rubio section in Spain showed virtually no change in MAAT and MAP values reconstructed with pedotransfer functions (Sheldon and others, 2012). One bulk geochemical index did indicate a decline in chemical weathering, which is suggestive of possible environmental change during deposition (Sheldon and others, 2012). A change in temperature seasonality could explain this change in weathering in the absence of a significant change in MAP or MAAT.

Clumped isotope temperatures from paleosol carbonate collected at the Maians-Rubio section range between 26 to 42 °C (excluding one significantly warmer outlier, MC-20; fig. 8). These temperatures are notably warmer than present-day, where mean

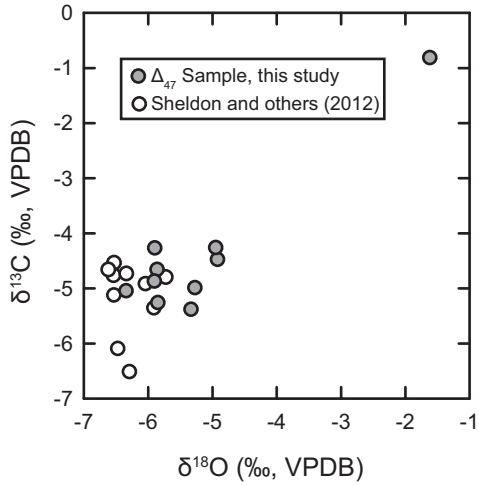

Fig. 9. $\delta^{18}O$ vs. $\delta^{13}C$ plot of paleosol carbonate samples. Gray circles represent samples analyzed for Δ_{47} composition in this study. White circles plot additional pedogenic carbonate samples analyzed for $\delta^{18}O$ and $\delta^{13}C$ in Sheldon and others (2012).

annual and warm month mean air temperatures are approximately 13 and 23 °C, respectively (Fick and Hijmans, 2017). Warmer than modern temperatures are expected because global temperatures during the Paleogene are generally understood to be warmer than present-day (Cramer and others, 2009), and the Maians-Rubio section was located further south during deposition by a few degrees latitude (Barberà and others, 2001).

However, fluctuations of 16 °C in MAAT (or warm-season temperature) are much too large during a time interval when the stacked $\delta^{18}O$ records from benthic foraminifera (Zachos and others, 2008) and paleotemperature reconstructions from other paleosol-bearing successions (Retallack, 2007; Gallagher and Sheldon, 2013) are virtually flat. This magnitude of temperature variation dwarfs the cooling reconstructed during the major global climate transition across the Eocene-Oligocene boundary. Terrestrial records from the continental interior of North America indicate 7 to 8 °C of cooling across the E-O boundary (Zanazzi and others, 2007; Fan and others, 2017), whereas ocean temperature estimates only indicate cooling between 3 to 5 °C (Liu and others, 2009). The large range in clumped isotope temperatures from the Maians-Rubio section could instead be explained by either a shift in the season of carbonate formation or by post-depositional processes reset the original formation temperatures.

The clumped isotope composition of paleosol carbonate can be reset to elevated temperatures if there was dissolution and reprecipitation in association with a warm fluid during burial (Huntington and others, 2011). Care was taken when drilling the samples to avoid any areas that displayed textural evidence of recrystallization in thin-section (for example, spar filled cracks). There is not an obvious relationship between the bulk $\delta^{18}O$ and $\delta^{13}C$ values indicative of interaction with post-depositional fluids (Lohmann, 1988). Only the stratigraphically uppermost sample (MC-20) is a clear outlier in terms of bulk $\delta^{18}O$ and $\delta^{13}C$ values (fig. 9), with both values exceeding all other samples by $>$ 3 permil. The remaining samples have $\delta^{13}C$ values consistent with a C_3-only plant assemblage (C_4 plants did not evolve until ~30 Ma ago; Edwards and others, 2010) and $\delta^{18}O$ values consistent with the site's proximity to the Mediterra-

nean Ocean and a seawater meteoric water source for precipitation (for example, Sheldon, 2018).

MC-20 also produced a clumped isotope temperature (58 °C) that greatly exceeds the other samples. While the bulk of the calcite in MC-20 is micritic, the sample contains more quartz, feldspar, and lithics relative to other samples analyzed (figs. 7D–7E). The coarser texture of the surrounding beds may have facilitated flow of early diagenetic fluids; however, this is speculative. In the absence of any clear trend between $\delta^{18}O$ and $\delta^{13}C$ values (fig. 9) or textural evidence among the remaining samples, only the Δ_{47} temperature of the uppermost sample (MC-20) is conclusively altered.

Clumped isotope temperatures can also be reset to elevated temperatures due to reordering of carbonate bonds within the crystal lattice (for example, Shenton and others, 2015; Gallagher and others, 2017). Heating experiments have suggested that carbonate clumped isotope signatures are likely stable on geologic timescales assuming that burial temperatures do not exceed 75 to 100 °C (Henkes and others, 2014; Stolper and Eiler, 2015). Maximum burial estimates of the Artés Formation derived from vitrinite reflectance data (Waltham and others, 2000) and numerical modeling (Garcia-Castellanos and others, 2003) indicate that the maximum burial depth of the Maians-Rubio section did not exceed one kilometer. Therefore, the large range in clumped isotope temperatures is not likely explained by solid-state reordering of some samples, because burial temperatures remained well below the reordering threshold.

In the absence of any clear evidence of post-depositional alteration, a shift in the season of carbonate formation is left as the most likely explanation. The plausibility of this explanation can be investigated using the same temperature model described above. Beginning with the assumption that carbonate always formed during the warm season, a corresponding MAST can be estimated for each paleosol sample assuming seasonal temperature variation of 15 to 25 °C (fig. 8A). The depth to the top of the paleosol was measured for each carbonate sample, and while uncertainty exists due to possible erosion of the uppermost part of the paleosols, these depths provide a minimum soil depth of carbonate formation. The magnitude of thermal damping for each paleosol is then calculated using average thermal conductivity and volumetric heat capacity values.

The minimum MAAT and air temperature seasonality values required to encompass the absolute range of observed clumped isotope temperatures can be calculated if the coldest samples (those within ±1 S.E. of the coldest sample – MC-18) are assumed to have formed during the spring or fall. Their average Δ_{47} temperature provides an estimate of 29 °C for MAST. If the remaining samples formed during the warm season, then at least 25 °C of seasonal air temperature variation is required for their calculated MAST values to fall at or below 29 °C (fig. 8B). The magnitude of ground-heating can be approximated using $PPM_{1.0}$ (Stinchcomb and others, 2016) estimates of MAP for the Maians-Rubio section, which ranged between 210 to 970 mm (bulk geochemistry data from Sheldon and others, 2012). Considering only SCAN sites that formed within this MAP range, the predicted ground heating effect is +2 °C with a standard deviation of 3 °C. Therefore, the estimated MAAT during the late Eocene at the Maians-Rubio section is 27 ± °3. This estimate, while significantly warmer than modern-day values at the Maians-Rubio section, compare favorably to contemporaneous temperature reconstructions from Western Europe. For example, average late Eocene (Priabonian) MAAT estimates derived from lacustrine gastropod shells collected at a higher latitude site on the Isle of Wight averaged 24 °C (Hren and others, 2013).

This explanation does necessitate local environmental change during the late Eocene that would cause the season of carbonate formation to shift. For example, seasonal hydrology patterns in Northern Spain may have changed leading up to the

E-O transition. There is some suggestion of environmental change from bulk geochemistry estimates of MAP generated with the $PPM_{1.0}$ model (fig. 8C). Time-averaged estimates increase up-section from 400 to 650 mm. Increasing MAP offers a potential explanation for the decrease in Δ_{47} temperatures observed in the five samples interpreted as MAST (fig. 8B). As discussed above, higher MAP values could lead to more vegetative cover and reduce the amount of ground-heating. However, the $PPM_{1.0}$ model may not be appropriate for paleosols from the Maians-Rubio section, as time-averaged MAAT estimates (10–14 °C) are colder than modern MAAT (15 °C).

While this preliminary interpretation of seasonality change should be tested further, it is, at present, the most reasonable explanation for the large range of observed clumped isotope temperatures. Regardless of the exact mechanism driving the spread in clumped isotope temperatures, the data from the Maians-Rubio section demonstrate how seasonality can be more thoroughly evaluated in paleosols by accounting for the processes that cause soil temperature to deviate from air temperature.

Broader Implications for Paleosol-Based Records

When reconstructing surface temperatures from paleosols, it is essential to consider the various processes that drive systematic deviations between soil and air temperature seasonality. Most of these processes are ultimately controlled by regional hydrology, albeit indirectly. For example, the amount and seasonal timing of snowfall controls how insulated the soil surface is from the cold winter air, and the magnitude of ground heating is controlled by the abundance of vegetation cover, which becomes sparser in drier environments. Therefore, simultaneous assessments of paleoprecipitation are needed to provide proper context for paleosol-based temperature reconstructions.

The context provided by paleo-hydrology reconstructions is especially important for temperature estimates derived from paleosol carbonate. There are two particular questions that need to be considered when estimating surface temperatures from paleosol carbonate: (1) how much annual precipitation did the site receive, and (2) during what season did the carbonate form?

As previously discussed, annual precipitation totals are related to the amount of additional ground heating caused by direct solar irradiation of the soil surface. A uniform ground-heating effect cannot be presumed for all paleosol carbonate. Only if the site is thought to be especially dry (MAP $<$ 300), should a large ground-heating effect (4–5 °C) be considered likely. For the majority of paleosols, a ground heating effect of ~2 °C is considered more appropriate.

The seasonal timing of paleosol carbonate formation also must be considered, because it determines whether or not thermal damping with soil depth must also be accounted for when interpreting measured temperatures. If soil carbonate is thought to have formed during the warmest season of the year, then thermal damping must be factored into estimates of warm season air temperature. For example, at 100 cm depth in the soil, the difference between mean annual and warm season temperature is ~36 percent less than that at the soil surface. Put another way, a warm-season carbonate nodule from 100 cm depth that produced a temperature of 6 °C above estimated MAAT, would correspond to a surface warm season temperature of closer to 10 °C above MAAT.

Thermal damping is less important if paleosol carbonate is interpreted as having formed during spring or fall, because soil temperatures at depth will fall close to mean annual values. In this situation, processes that cause deviations between MAST and MAAT, such as ground heating and snow insulation, would still need to be considered. Ground heating should always be factored into soil carbonate derived air temperature estimates, regardless of the seasonal timing of soil carbonate formation. This correc-

tion applies even in settings where there is strong seasonal variation in the amount of solar radiation that reaches the soil surface (for example sites at high latitudes). In these settings, there would be a large ground heating effect during the summer, and little effect during the winter. Regardless, an increase in warm season surface temperature alone will cause an increase in MAST.

CONCLUSIONS

Systematic deviations of soil temperature seasonality from air temperature seasonality provide important context for temperature reconstructions from paleosols. Within the compiled SCAN dataset, nearly half of the soils experience larger temperature seasonality than is predicted based on seasonal air temperature patterns alone. In contrast, two-fifths experience less temperature seasonality than is predicted.

Sites that experienced more temperature seasonality than predicted are best explained by the effect of direct heating of the soil surface by solar radiation, which elevates the soil surface temperature above that of the overlying air. Across all of the sites, the average ground heating is 2.2 °C. The ground heating effect is more pronounced at sites that receive less than 600 mm of annual precipitation, likely due to a reduction in vegetative cover. Generally, the magnitude of this effect is closer to and not as consistently large as earlier studies had suggested. It is only at the driest sites (MAP $<$ 300 mm) that the average ground heating effect exceeds 4 °C. Therefore, independent reconstructions of MAP are needed to place surface temperature estimates derived from paleosol carbonate geochemical data in the proper climate context. This consideration is particularly important for records spanning major climate transitions, where shifts in regional hydrology patterns may accompany changes in surface temperatures.

Approximately two-fifths of modern sites examined here experienced less soil temperature seasonality than expected. The reduction in soil temperature seasonality is directly related to the cold month air temperature and is likely explained by insulation from snow cover. Warmer than expected soil temperatures would allow for more rapid chemical weathering, offering an explanation for the consistent breakdown of bulk paleosol geochemistry temperature proxies at sites with MAAT $<$ 6 °C.

The paleosol carbonate record from the Maians-Rubio section that demonstrates the importance of considering these systematic deviations in soil temperature seasonality when evaluating paleosol temperature reconstructions. Because there is no evidence of diagenetic alteration or deep burial of the paleosols, the large spread in clumped isotope temperatures (16 °C) is best explained by shifts in the season of soil carbonate formation. Assuming that the nodules with the coldest Δ_{47} temperatures formed in the spring or fall, the estimated MAAT in Northern Spain during the late Eocene is 27 $\pm$ 3 °C with seasonal temperature variation of at least 25 °C. This interpretation necessitates changes in regional hydrology that would have shifted the season of soil carbonate formation.

ACKNOWLEDGMENTS

This material is based upon work supported by the National Science Foundation Graduate Student Research Fellowship under Grant No. DGE 1256260 to TMG and support from the Thomas Holloway Foundation to NDS. This manuscript was improved thanks to the thoughtful comments of two anonymous reviewers.

APPENDIX

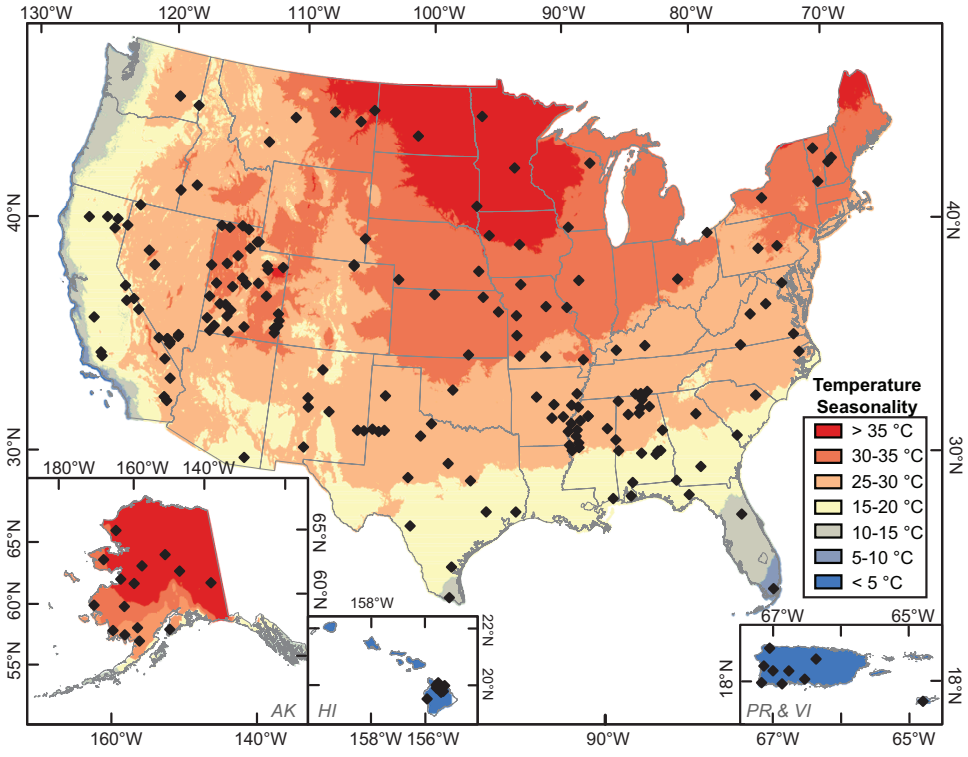

Fig. A1. Map of Soil Climate Analysis Network (SCAN) sites where colors represent the normal air temperature seasonality (warmest month average air temperature – coldest month average air temperature). Black diamonds represent SCAN sites. Temperatures for the contiguous United States are from the PRISM data set (PRISM Climate Group, 2015). Temperatures for Alaska, Hawaii, Puerto Rico and the Virgin Islands are interpolated from the 1981–2010 US climate normals dataset (Arguez and others, 2012).

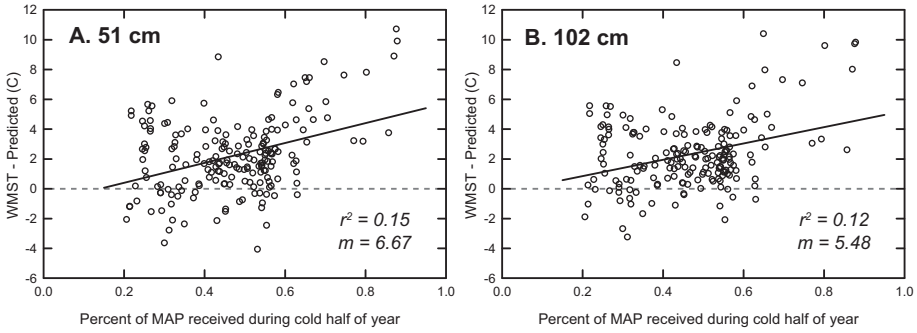

Fig. A2. Percent of mean annual precipitation (MAP) received during the coldest 6 months vs. the difference between observed and predicted warm month mean soil temperatures (WMST) at the SCAN sites. (A) 51 cm data. (B) 102 cm data.

TABLE A1

Compiled SCAN and climate data

Site#	Site Name	State	Flags			Soil Temp. (Max-Min)		Air Temp. (Max-Min)	CMAT	MAP	WMST-Perdicted		CMST-Perdicted	
			20 in	*40 in*	*AirT*	*20 in*	*40 in*	*°C*	*°C*	*mm*	*20 in*	*40 in*	*20 in*	*40 in*
2021	Lind #1	WA				20.6	15.8	23.1	-1.7	249	4.6	4.1	2.3	2.8
2198	Cook Farm Field D	WA				17.0	13.3	20.4	-1.6	506	3.1	2.8	2.3	2.4
2074	Lynhart Ranch	OR				19.0	15.8	19.6	1.0	478	3.2	3.0	-0.1	-0.3
2218	French Gulch	CA				18.5	14.1	19.5	4.7	1654	3.8	2.6	0.8	0.8
2214	Ash Valley	CA				21.6	22.6	19.3	-1.3	278	7.4	10.4	1.3	0.0
2192	Eagle Lake	CA				22.1	18.0	19.7	-1.6	421	7.6	7.1	1.2	1.6
2215	Bodie Hills	CA				14.8	11.9	18.5	-2.9	509	3.2	3.3	3.0	3.1
2149	Marble Creek	CA				19.5	17.2	20.2	0.3	225	7.2	8.0	3.7	3.5
2191	Doe Ridge	CA				17.5	12.5	18.9	-1.6	341	7.8	9.6	5.3	9.0
2187	Deep Springs	CA				22.2	17.2	22.1	0.3	162	6.5	5.9	1.8	2.6
2217	Monocline Ridge	CA				22.7	16.9	17.5	8.2	226	10.7	9.7	1.8	3.9
2190	Death Valley Jct	CA				24.4	19.6	22.5	7.3	109	8.5	7.3	2.0	2.0
2186	Shadow Mtns	CA				22.4	17.4	23.3	5.6	171	5.8	4.8	1.8	2.1
2189	Cochora Ranch	CA				19.4	15.3	16.7	8.4	216	9.9	9.8	3.7	5.0
2219	Stubblefield	CA				20.0	13.7	16.8	7.0	237	8.9	8.0	2.3	5.0
2185	Essex	CA				22.3	19.6	22.1	8.6	185	7.0	6.9	2.3	1.3
2183	Desert Center	CA		X		22.1	-	21.4	12.3	78	7.5	-	2.4	-
2184	Ford Dry Lake	CA				19.5	13.6	21.6	12.3	85	5.4	5.0	3.0	4.9
674	Orchard Range Site	ID		X		22.9	-	24.1	-1.3	290	4.8	-	1.1	-
2148	Jordan Valley Cwma	ID	X	X		-	-	22.9	-2.5	347	-	-	-	-
750	Sheldon	NV		X		16.5	-	20.3	-2.8	260	6.3	-	6.0	-
2216	Buckhorn	NV		X		18.8	-	19.5	-2.2	461	5.8	-	2.5	-
2116	Lovelock NNR	NV				18.4	11.0	24.3	-0.5	136	2.5	0.7	3.4	5.0
2170	Porter Canyon	NV				18.3	13.4	21.6	-1.5	342	2.7	1.6	1.5	1.9
2143	Hayford Peak	NV		X		16.3	-	18.9	-2.8	423	1.9	-	0.6	-
2144	Pine Nut	NV				16.4	13.4	20.9	1.3	352	2.2	2.3	2.4	2.0
2145	Charkiln	NV				16.0	12.3	19.7	1.5	429	-0.4	-0.7	-0.7	-0.6
2142	Trough Springs	NV				15.1	10.8	19.5	0.4	446	1.1	0.2	1.5	1.7
2141	Kyle Canyon	NV				19.4	16.5	19.3	0.8	554	4.6	4.6	0.5	0.2
2146	Lovell Summit	NV	X	X		-	-	20.0	1.5	420	-	-	-	-
2160	Grouse Creek	UT				18.4	15.5	24.5	-4.1	322	3.6	4.1	4.6	4.1
2153	Park Valley	UT				21.4	16.2	25.6	-3.6	273	4.2	3.8	3.2	3.8
2135	Blue Creek	UT				20.4	15.7	26.7	-5.5	414	4.6	3.9	5.5	5.1
2136	Cache Junction	UT				16.5	12.6	27.1	-4.6	427	-1.3	-1.2	3.9	3.4
2151	Buffalo Jump	UT		X		17.6	-	24.9	-6.8	307	3.2	-	5.3	-
2150	Chicken Ridge	UT				15.2	12.0	22.9	-5.3	663	1.7	1.8	4.7	4.3
2133	Morgan	UT				18.6	16.2	25.6	-3.5	486	0.7	1.2	2.4	1.2
2152	Grantsville	UT				17.7	13.3	27.0	-1.6	366	1.1	1.6	4.8	5.3
2154	Split Mountain	UT				25.3	20.3	31.2	-7.7	218	3.9	3.7	3.4	3.1
2134	Mountain Home	UT				16.1	12.9	25.6	-6.3	290	1.2	1.5	5.4	4.7
2155	Little Red Fox	UT				21.1	16.7	28.9	-6.7	220	1.6	1.5	3.5	3.1
2167	Dugway	UT				21.2	19.5	28.3	-2.6	210	1.3	2.8	2.6	1.1
2165	Goshute	UT				21.4	16.3	24.2	-2.6	271	3.6	3.6	1.5	2.6
2137	Nephi	UT				19.9	16.1	25.7	-2.6	401	2.4	2.3	2.9	2.4
2132	Price	UT				24.6	20.4	26.7	-3.7	235	4.6	4.8	1.2	1.3
2126	Ephraim	UT				17.5	14.2	25.5	-3.4	329	0.1	0.6	2.9	2.6
2163	Tule Valley	UT				29.2	23.8	27.5	-2.7	188	8.8	8.5	1.5	2.0
2127	Holden	UT				23.2	18.3	26.9	-2.9	261	4.0	4.3	2.2	3.0
2131	Green River	UT				30.6	24.4	28.8	-2.2	171	5.7	5.3	-2.0	-0.9
2164	Hals Canyon	UT				22.8	17.7	25.4	-2.0	177	3.9	3.8	1.4	2.2
2129	Milford	UT				19.6	15.1	26.1	-2.2	268	2.0	2.0	3.0	3.4
2156	Manderfield	UT				18.7	14.8	23.2	-2.1	330	2.3	2.1	2.1	1.9
2125	Circleville	UT				19.6	14.0	23.2	-2.2	239	1.9	1.6	0.8	2.3
2166	Harms Way	UT				20.2	15.6	24.4	-2.9	392	3.2	2.7	2.5	2.6
2139	West Summit	UT				20.6	16.7	23.9	-2.6	399	2.9	2.8	1.2	1.2
2130	Eastland	UT				18.3	15.4	24.0	-2.5	388	2.1	2.8	2.8	2.4
2138	Alkali Mesa	UT				21.1	18.9	24.3	-1.5	372	3.3	4.0	1.5	0.4
2140	Mccracken Mesa	UT				22.3	18.3	25.9	-0.7	268	3.0	3.8	1.3	1.8
2158	Spooky	UT				22.5	18.6	25.2	0.2	212	2.7	2.0	0.1	-0.8
2157	Panguitch	UT				15.9	10.7	22.8	-2.8	255	-0.6	-1.0	1.5	2.6
2162	Vermillion	UT				18.8	15.2	23.0	-1.3	335	1.5	1.4	0.9	0.7
2161	Cave Valley	UT				21.2	18.0	21.8	-0.5	420	4.3	3.9	0.5	-0.3
2128	Enterprise	UT				21.7	16.4	24.2	-1.3	317	4.0	3.6	1.5	2.5
2159	Sand Hollow	UT				25.1	19.8	23.5	5.3	284	4.0	3.4	-2.4	-1.6
2026	Walnut Gulch #1	AZ				16.0	11.9	18.4	8.0	338	3.6	3.8	2.2	3.5

TABLE A1

(continued)

Site#	Site Name	State	Flags			Soil Temp. (Max-Min)		Air Temp. (Max-Min)	CMAT	MAP	WMST-Perdicted		CMST-Perdicted	
			20 in	*40 in*	*AirT*	*20 in*	*40 in*	*°C*	*°C*	*mm*	*20 in*	*40 in*	*20 in*	*40 in*
2019	Fort Assinboine #1	MT				19.0	15.2	28.1	-7.7	325	2.5	2.4	5.9	5.1
2118	Violett	MT				22.1	17.5	26.0	-6.3	267	4.5	4.2	3.1	3.1
2117	Conrad Ag Rc	MT				19.3	15.1	23.8	-5.1	306	3.0	3.0	2.7	2.9
2120	Sidney	MT				19.5	15.8	30.7	-9.3	360	0.2	0.6	5.2	4.2
581	Lindsay	MT				20.1	16.2	29.0	-7.8	335	2.0	2.0	4.8	4.1
2121	Jordan	MT				22.9	19.3	28.0	-5.9	352	2.7	3.4	2.0	1.8
2119	Mioccasin	MT				16.9	14.8	22.3	-3.7	388	2.8	3.3	3.6	2.7
808	Table Mountain	MT				18.0	13.8	23.9	-4.3	321	2.0	1.5	3.1	2.9
2018	Torrington #1	WY				22.8	18.4	25.8	-2.9	361	4.2	4.3	1.9	2.2
2017	Nunn #1	CO				21.5	17.6	24.0	-2.6	352	4.4	4.9	2.0	2.5
2197	CPER	CO				22.6	18.5	24.2	-2.5	341	4.4	4.1	1.1	0.9
2172	Alcade	NM				24.4	18.5	22.8	0.0	277	5.9	4.7	-0.4	0.6
2169	Los Lunas PMC	NM				20.5	17.2	23.6	1.7	243	3.1	3.8	1.4	1.5
2171	Sevilleta	NM				23.1	18.6	22.8	2.1	284	5.5	5.5	0.5	1.3
2015	Adams Ranch #1	NM				19.6	15.8	20.1	1.8	393	4.6	4.2	1.0	1.1
2108	Willow Wells	NM				22.5	19.7	21.1	4.1	408	5.2	5.6	-0.5	-0.8
2107	Crossroads	NM				22.0	17.2	21.2	4.3	402	4.9	5.0	-0.3	1.2
2168	Jornada Exp Range	NM				21.3	15.9	21.6	4.7	271	5.2	5.0	1.1	2.7
2020	Mandan #1	ND				16.7	12.3	31.7	-10.4	455	-2.1	-1.9	6.5	5.9
2072	Eros Data Center	SD				19.6	16.3	31.3	-9.0	684	-0.3	0.1	4.9	3.6
2001	Rogers Farm #1	NE				19.9	16.2	28.9	-4.2	788	-0.3	-0.2	2.9	1.9
2111	Johnson Farm	NE				20.6	16.6	26.5	-2.2	492	0.7	1.0	1.2	1.1
2093	Phillipsburg	KS				20.0	16.3	28.1	-2.2	615	0.1	0.5	2.5	2.0
2094	Centralia Lake	KS				17.6	14.0	28.0	-2.7	875	-1.5	-0.8	3.1	2.9
2147	Ku-Nesa	KS				19.8	15.7	27.3	-1.4	992	-0.4	-0.1	1.5	1.5
2092	Abrams	KS				20.1	17.3	26.1	1.1	954	0.1	1.2	0.7	0.4
2022	Fort Reno #1	OK				16.9	13.9	24.5	3.4	868	-2.4	-1.7	0.2	-0.1
2006	Bushland #1	TX				18.3	14.8	22.8	2.3	500	1.2	1.6	1.0	1.3
2202	Vernon	TX	X	X		-	-	24.0	5.2	709	-	-	-	-
2201	Knox City	TX				24.7	20.2	22.7	6.3	647	4.0	4.0	-2.7	-1.9
2104	Reese Center	TX				20.9	16.8	21.6	4.5	513	3.9	3.6	0.1	0.5
2105	Levelland	TX				21.0	16.9	21.7	4.2	503	4.0	4.0	0.4	0.9
2106	Lehman	TX				21.6	18.1	21.6	3.9	469	5.7	5.6	1.2	1.1
2203	Stephenville	TX				19.9	15.9	20.8	7.3	817	1.8	1.9	-1.6	-0.9
2200	San Angelo	TX				20.4	15.6	20.5	7.5	568	3.7	3.5	-0.4	0.9
2199	Riesel	TX				17.3	13.3	20.7	8.4	946	1.6	1.4	0.8	1.2
2207	Beaumont	TX				16.6	12.8	17.6	10.7	1482	1.5	1.3	-1.2	-0.3
2016	Prairie View #1	TX				14.4	12.0	18.5	10.4	1123	0.8	1.1	1.1	0.8
2204	Uvalde	TX				15.4	11.9	18.6	10.5	600	-0.1	1.6	-0.8	1.4
2206	Kingsville	TX				15.5	11.5	16.0	13.8	738	1.4	0.6	-1.4	-0.9
2205	Weslaco	TX	X	X		-	-	14.6	15.5	599	-	-	-	-
2050	Glacial Ridge	MN				17.2	13.9	34.2	-14.1	594	-1.2	0.2	8.8	7.9
2002	Crescent Lake #1	MN				18.4	15.8	32.5	-10.8	755	-1.5	-0.1	5.9	4.6
2068	Shagbark Hills	IA				20.4	15.9	30.3	-7.2	770	0.3	0.3	3.9	3.5
2031	Ames	IA				14.5	12.2	29.9	-6.8	919	-3.6	-2.7	5.6	4.0
2047	Spickard	MO				18.6	15.3	28.3	-3.8	986	0.0	0.6	4.0	3.3
2061	Powell Gardens	MO				18.6	15.9	26.9	-1.5	1098	0.5	1.4	3.4	2.5
2195	CMRB LTAR-MO	MO				20.6	15.8	26.9	-1.8	1046	0.3	0.2	1.1	1.4
2220	Elsberry PMC	MO	X	X		-	-	26.7	-1.4	1021	-	-	-	-
2193	Schell-Osage	MO				18.7	15.1	26.3	-0.5	1145	0.2	0.3	2.4	1.8
2060	Mt Vernon	MO				19.2	16.7	24.9	0.5	1159	1.2	2.3	1.8	1.4
2194	Journagan Ranch	MO				18.3	16.4	24.4	0.5	1158	-0.9	0.6	0.2	-0.4
2048	Dexter	MO				20.4	17.1	25.2	1.6	1228	1.5	1.8	1.1	0.5
2085	Uapb-Earle	AR				21.6	16.8	23.5	3.7	1285	3.3	2.5	0.3	0.6
2090	Uapb Point Remove	AR				19.3	16.4	23.1	4.1	1260	1.9	2.2	1.0	0.4
2030	Uapb-Lonoke Farm	AR				18.5	15.5	23.0	4.6	1270	1.2	1.1	1.0	0.1
2084	Uapb-Marianna	AR				20.0	16.7	23.2	4.2	1293	2.5	2.6	0.9	0.5
2091	Uapb Dewitt	AR				19.8	17.1	22.3	5.3	1284	2.3	2.8	0.3	-0.3
2083	Uapb Campus-PB	AR				18.3	15.8	22.3	5.4	1334	1.7	2.1	1.1	0.3
2003	Wabeno #1	WI				12.8	10.7	29.4	-10.5	781	-2.1	-1.0	8.5	6.8
2196	UW Platteville	WI				19.2	15.3	29.6	-7.5	925	-0.5	-0.2	3.7	3.1
2004	Mason #1	IL				20.6	18.5	28.0	-3.6	975	1.3	2.4	3.0	1.6
2034	Tunica	MS				17.9	14.2	23.0	4.5	1350	0.2	0.9	0.5	1.1
2024	Goodwin Ck Pasture	MS				16.4	14.2	22.2	4.7	1407	-0.4	1.1	0.8	1.0
2025	Goodwin Ck Timber	MS				13.3	11.0	22.2	4.7	1407	-2.5	-2.1	1.9	0.9

TABLE A1
(continued)

Site#	Site Name	State	Flags			Soil Temp. (Max-Min)		Air Temp. (Max-Min)	CMAT	MAP	WMST-Perdicted		CMST-Perdicted	
			20 in	*40 in*	*AirT*	*20 in*	*40 in*	*°C*	*°C*	*mm*	*20 in*	*40 in*	*20 in*	*40 in*
2035	Vance	MS				19.0	16.6	22.4	5.1	1373	1.5	2.1	0.3	-0.3
2046	Perthshire	MS				19.9	15.7	22.2	5.4	1330	2.7	2.3	0.4	0.6
2064	Starkville	MS				17.7	14.6	21.4	5.8	1418	1.9	1.9	1.2	0.8
2109	Sandy Ridge	MS				22.6	19.9	21.9	5.9	1376	4.8	5.1	-0.4	-1.0
2070	Scott	MS				20.6	17.0	22.0	5.8	1321	3.9	3.6	0.7	0.4
2032	Beasley Lake	MS				18.0	14.7	21.7	6.2	1373	1.8	1.3	1.1	0.2
2086	Silver City	MS				17.5	14.3	21.1	6.6	1387	0.5	1.0	-0.2	0.1
2087	North Issaquena	MS				18.1	13.4	21.3	6.7	1420	2.3	1.7	1.2	1.8
2110	Mayday	MS				16.4	12.6	20.7	7.1	1407	0.1	0.0	0.2	0.5
2033	Onward	MS				18.0	14.3	20.6	7.0	1444	2.4	2.0	0.8	0.7
2082	Tnc Fort Bayou	MS				12.7	11.1	17.3	10.5	1705	0.3	0.9	1.3	0.8
2005	Princeton 1	KY				17.3	15.4	23.9	2.2	1263	-0.3	0.5	1.2	0.2
2079	Mammoth Cave	KY				18.3	15.4	23.3	1.7	1290	1.3	1.0	1.5	0.3
2077	Eastview Farm	TN				16.8	14.1	21.2	3.8	1401	0.4	0.7	0.6	0.1
2075	McAllister Fram	TN				18.3	15.0	21.8	3.7	1448	1.7	1.5	0.8	0.2
2076	Allen Farms	TN				16.0	12.9	21.9	3.8	1441	-1.0	0.1	0.4	1.1
2053	Wtars	AL				17.4	11.8	21.8	3.9	1430	1.6	0.5	1.5	2.5
2078	Bragg Farm	AL				17.6	14.9	21.8	4.0	1420	1.5	1.5	1.2	0.3
2057	AAMU-JTG	AL				17.7	15.0	21.8	4.0	1440	1.1	1.4	0.7	0.1
2173	Isbell Farms	AL				20.0	16.0	21.9	4.3	1453	2.9	2.2	0.2	0.0
2055	Hodges	AL				17.7	14.0	21.4	4.7	1376	1.2	0.9	0.4	0.3
2056	Stanley Farm	AL				15.9	14.4	21.4	4.6	1475	-0.3	1.1	0.8	0.2
2113	Cullman-NAHRC	AL				18.2	16.1	21.0	4.7	1504	3.1	3.4	1.4	0.5
2179	Sudduth Farms	AL				18.3	16.1	21.3	4.5	1516	1.8	2.6	0.6	-0.1
2175	Wedowee	AL				16.9	15.6	20.0	5.7	1363	3.0	3.8	2.0	0.8
2174	Dee River Ranch	AL				16.8	13.9	21.4	6.0	1372	0.7	1.2	0.9	0.9
2114	Livingston-UWA	AL				16.9	14.7	20.2	7.1	1381	2.5	2.8	1.6	0.9
2176	Selma	AL				17.9	15.3	19.6	8.1	1328	2.6	3.0	0.3	0.1
2177	Broad Acres	AL				16.6	13.4	19.4	8.0	1321	2.2	2.0	1.1	0.8
2178	Morris Farms	AL				19.1	13.6	19.5	8.0	1327	3.4	2.0	-0.2	0.7
2115	Tuskegee	AL				17.8	15.3	19.5	7.5	1327	3.9	4.0	1.6	1.0
2182	River Road Farms	AL				14.2	12.1	17.9	10.2	1379	0.5	1.1	0.5	0.3
2181	Perdido Riv Farms	AL				15.8	13.5	18.0	9.2	1609	1.4	2.0	-0.1	-0.2
2180	Koptis Farms	AL				15.5	13.3	17.5	9.9	1728	2.5	2.9	1.0	0.7
2073	Sunleaf Nursery	OH				19.7	16.5	24.8	-2.6	1040	1.0	1.8	1.1	1.0
2014	Molly Caren 1	OH				17.4	14.1	25.7	-2.5	999	0.3	0.4	3.4	2.6
2013	Watkinsville 1	GA				16.4	14.3	20.4	6.1	1220	0.4	1.0	0.3	-0.4
2027	Little River	GA				16.5	13.5	18.1	9.4	1190	2.4	2.5	0.4	0.5
2009	Wakulla 1	FL				13.5	11.2	17.0	10.6	1520	0.6	0.8	0.5	0.3
2012	Sellers Lake 1	FL				12.9	11.7	14.0	13.8	1341	2.8	3.7	1.1	0.8
2051	Everglades ARS	FL	X	X		-	-	9.1	19.1	1403	-	-	-	-
2069	Hubbard Brook	NH				12.7	10.5	27.7	-9.1	1238	-1.4	-0.4	8.0	6.6
2043	Mascoma River	NH				12.5	10.4	27.3	-8.4	1120	-2.1	-1.1	7.0	5.7
2041	Mount Mansfield	VT				12.2	10.2	28.0	-10.3	1843	-1.5	-0.3	8.6	7.2
2042	Lye Brook	VT				12.1	9.9	25.5	-8.5	1768	-0.7	0.0	7.4	6.2
2011	Geneva 1	NY				17.0	14.5	25.8	-4.2	859	1.1	1.4	4.5	3.1
2036	Rock Springs Pa	PA				18.3	15.4	24.8	-3.4	1044	1.7	1.5	3.1	1.7
2028	Mahantango Ck	PA				20.6	18.8	25.2	-3.2	1125	2.8	4.1	2.2	1.2
2049	Powder Mill	MD				19.9	15.6	24.3	0.7	1093	1.6	0.3	1.0	0.0
2039	N Piedmont Arec	VA				19.9	15.7	22.9	1.6	1103	3.0	2.5	1.3	1.3
2088	Shenandoah	VA				18.0	15.0	22.4	0.2	1096	1.4	2.2	1.2	1.3
2040	Tidewater Arec	VA				17.6	16.3	21.9	4.2	1231	1.7	2.4	1.5	-0.1
2089	Reynolds Homestead	VA				18.6	16.4	21.9	2.7	1217	1.9	2.5	0.6	-0.1
2008	Tidewater 1	NC				17.4	14.1	20.6	6.0	1293	1.9	1.8	0.9	0.6
2037	Pee Dee	SC				17.2	15.2	20.7	6.6	1175	2.2	2.7	1.4	0.6
2038	Youmans Farm	SC				16.2	13.6	19.0	8.8	1204	1.7	2.0	0.6	0.3
2052	Isabela	PR		X		4.2	-	3.4	23.3	1650	1.7	-	0.2	-
2188	Corozal	PR				3.1	2.6	3.8	22.8	1975	0.3	0.4	0.2	0.2
2112	Mayaguez TARS	PR	X	X	X	-	-	-	-	-	-	-	-	-
15	Maricao Forest	PR				1.7	1.2	3.0	20.3	2307	-1.0	-0.6	-0.4	0.1
2045	Guilarte Forest	PR			X	2.5	1.8	-	-	-	22.5	21.4	20.1	19.6
2122	Fortuna	PR				4.7	3.6	3.2	24.8	977	2.7	2.2	0.6	0.8
2067	Bosque Seco	PR	X	X	X	-	-	-	-	-	-	-	-	-
2066	Combate	PR				4.6	3.1	3.7	23.6	1219	2.3	2.0	0.6	1.2
2123	Upper Bethlehem	VI				2.9	2.2	3.1	25.7	982	0.8	0.7	0.3	0.5

TABLE A1
(continued)

Site#	Site Name	State	Flags			Soil Temp. (Max-Min)		Air Temp. (Max-Min)	CMAT	MAP	WMST-Perdicted		CMST-Perdicted	
			20 in	*40 in*	*AirT*	*20 in*	*40 in*	*°C*	*°C*	*mm*	*20 in*	*40 in*	*20 in*	*40 in*
965	Ikalukrok Creek	AK		X	X	10.7	-	-	-	-	-2.5	-	10.0	-
2212	Kanuti Lake	AK	X	X	X	-	-	-	-	-	-	-	-	-
2213	Checkers Creek	AK			X	15.2	11.9	-	-	-	-5.0	-5.5	0.5	-0.9
2210	Hozatka Lake	AK	X	X	X	-	-	-	-	-	-	-	-	-
2081	Nenana	AK				14.1	9.7	37.2	-21.2	306	-0.8	0.0	14.7	13.8
2221	Unalakleet	AK	X	X	X	-	-	-	-	-	-	-	-	-
2211	Innoko Camp	AK	X	X	X	-	-	-	-	-	-	-	-	-
2080	Tok	AK				16.3	11.7	39.4	-24.1	240	-1.2	-1.0	13.8	12.1
2065	Aniak	AK			X	9.7	6.1	-	-	-	-3.1	-2.5	9.1	8.8
2208	Kanaryagak Camp	AK			X	5.8	3.5	-	-	-	-9.7	-8.5	6.4	5.4
2062	Moose Inc	AK		X		5.8	-	16.6	-4.0	618	-4.1	-	3.3	-
1233	Lower Mulchatna	AK			X	8.4	3.8	-	-	-	-5.0	-6.7	3.7	3.1
1232	Canyon Lake	AK			X	8.1	5.9	-	-	-	-3.2	-2.6	6.3	5.5
1234	Weary Lake	AK				10.6	9.0	22.2	-9.4	643	-0.2	0.7	6.8	5.8
2209	Naknek River	AK				8.0	5.3	21.8	-8.8	495	-2.8	-3.2	6.6	5.3
2097	Kukuihaele	HI				2.9	2.4	4.2	19.2	2368	0.4	0.6	0.8	0.9
2099	Waimea Plain	HI			X	1.7	1.3	-	-	-	19.5	19.3	17.8	18.0
2102	Mana House	HI			X	3.0	2.1	-	-	-	18.7	18.7	15.8	16.6
2103	Kemole Gulch	HI			X	2.4	1.9	-	-	-	19.4	20.4	17.0	18.5
2100	Island Dairy	HI				3.1	2.4	4.2	19.2	3720	-0.5	-0.6	-0.2	-0.3
2098	Pua Akala	HI		X	X	3.0	-	-	-	-	13.2	-	10.2	-
2101	Silver Sword	HI		X	X	5.0	-	-	-	-	14.6	-	9.6	-
2096	Kainaliu	HI		X		2.9	-	2.3	19.8	1270	2.8	-	1.7	-

AirT: Air Temperature.
CMAT: Cold Month Average Air Temperature.
MAP: Mean Annual Precipitation.
WMST: Warmest Month Average Soil Temperature.
CMST: Coldest Month Average Soil Temperature.

TABLE A2

Clumped isotope data – brand ^{17}O correction

Date	Name	Window	δ^{45}	δ^{46}	δ^{47}	δ^{48}	δ^{49}	$\delta^{13}C$	$\delta^{18}O$	Δ_{47}	Δ_{48}	Δ_{49}	$\Delta_{47\text{-SGvWG}}$	$\Delta_{47\text{-RF}}$	$\Delta_{47\text{-RF-AC}}$
May-June 2012															
6/11	MC-14	2	-1.39	-2.04	-3.96	-5.47	1.66	-5.00	33.23	-0.476	-0.721	6.378	-0.351	0.583	0.649
6/12	MC-15	2	-1.67	-1.99	-4.20	-5.47	1.22	-5.30	33.28	-0.477	-0.823	6.142	-0.344	0.590	0.656
6/12	MC-16	2	-1.49	-1.61	-3.62	-4.39	1.92	-5.13	33.67	-0.456	-0.497	5.906	-0.341	0.593	0.660
October-November 2012: Samples and Standards															
10/27	MC-14	1	-1.27	-1.85	-3.56	-4.73	1.03	-4.87	33.43	-0.399	-0.370	5.221	-0.310	0.607	0.673
10/27	MC-15	1	-1.67	-1.89	-4.03	-4.87	0.89	-5.30	33.39	-0.418	-0.430	5.597	-0.317	0.599	0.665
10/27	MC-16	1	-1.29	-1.16	-2.89	-2.93	0.77	-4.93	34.14	-0.372	0.062	3.639	-0.299	0.618	0.684
10/28	MC-14	1	-1.14	-1.80	-3.38	-4.90	1.00	-4.74	33.48	-0.393	-0.629	4.973	-0.308	0.608	0.675
10/28	MC-15	1	-1.55	-1.79	-3.77	-4.54	1.34	-5.18	33.50	-0.374	-0.304	5.725	-0.279	0.639	0.706
10/28	MC-16	1	-1.30	-1.17	-2.89	-2.77	0.51	-4.94	34.13	-0.361	0.241	3.404	-0.289	0.629	0.696
10/29	MC-18	1	-1.62	-2.49	-4.56	-6.31	0.81	-5.23	32.76	-0.400	-0.662	6.668	-0.286	0.632	0.699
10/30	MC-13	1	-0.96	-1.12	-2.53	-2.62	0.63	-4.58	34.19	-0.392	0.281	3.060	-0.328	0.586	0.653
10/30	MC-11	1	-1.72	-1.37	-3.56	-3.54	0.54	-5.38	33.93	-0.397	-0.139	4.268	-0.308	0.608	0.675
10/30	MC-15	1	-1.62	-1.89	-3.97	-4.88	0.89	-5.25	33.39	-0.408	-0.444	5.548	-0.309	0.608	0.674
10/30	MC-14	1	-1.26	-2.07	-3.79	-5.28	0.78	-4.87	33.20	-0.413	-0.469	5.417	-0.318	0.598	0.664
10/31	MC-16	1	-1.33	-1.29	-3.07	-3.26	0.77	-4.96	34.01	-0.395	-0.017	3.923	-0.318	0.597	0.664
11/2	MC-18	1	-1.34	-2.30	-4.11	-5.99	0.69	-4.94	32.96	-0.424	-0.724	5.868	-0.321	0.594	0.661
11/2	MC-13	1	-1.03	-1.40	-2.83	-3.37	-0.71	-4.64	33.89	-0.357	0.105	2.346	-0.286	0.632	0.698
11/10	MC-13	2	-0.90	-1.00	-2.35	-2.58	0.57	-4.51	34.31	-0.396	0.093	2.705	-0.329	0.548	0.615
11/10	MC-18	2	-1.37	-2.35	-4.16	-6.08	-0.14	-4.97	32.91	-0.390	-0.714	5.159	-0.272	0.610	0.676
11/11	MC-20	2	2.64	2.39	4.81	6.35	-0.30	-0.87	37.81	-0.225	2.228	-8.555	-0.361	0.514	0.581
11/11	MC-17	2	-0.32	-0.73	-1.47	-2.02	0.86	-3.91	34.59	-0.373	0.117	1.848	-0.332	0.546	0.612
11/11	MC-11	2	-1.81	-1.60	-3.92	-4.01	0.14	-5.47	33.70	-0.440	-0.151	4.417	-0.329	0.549	0.615
11/12	MC-9	2	-1.03	-1.81	-3.27	-4.60	0.27	-4.62	33.47	-0.390	-0.313	4.132	-0.298	0.582	0.649
11/12	MC-20	2	2.78	2.48	5.06	6.95	0.07	-0.72	37.90	-0.216	2.643	-8.512	-0.359	0.516	0.583
11/12	MC-11	2	-1.59	-1.21	-3.27	-2.79	-0.71	-5.24	34.10	-0.402	0.295	2.565	-0.310	0.569	0.636
11/12	MC-9	2	-1.02	-1.84	-3.28	-4.81	0.26	-4.61	33.44	-0.383	-0.474	4.164	-0.290	0.590	0.657
11/15	MC-18	2	-1.45	-2.71	-4.66	-6.94	0.58	-5.04	32.54	-0.457	-0.855	6.680	-0.326	0.552	0.619
11/16	MC-9	2	-1.15	-2.05	-3.63	-5.50	0.28	-4.75	33.22	-0.391	-0.742	4.755	-0.288	0.593	0.659
11/16	MC-11	2	-1.77	-1.31	-3.55	-3.45	0.50	-5.43	33.99	-0.395	-0.158	4.176	-0.295	0.586	0.652

TABLE A2
(continued)

Date	Name	Window	δ^{45}	δ^{46}	δ^{47}	δ^{48}	δ^{49}	$\delta^{13}C$	$\delta^{18}O$	Δ_{47}	Δ_{48}	Δ_{49}	$\Delta_{47\text{-SGvWG}}$	$\Delta_{47\text{-RF}}$	$\Delta_{47\text{-RF-AC}}$
October-November 2012: Samples and Standards															
11/16	MC-19	2	-0.68	-1.86	-2.97	-4.94	0.26	-4.25	33.41	-0.390	-0.549	3.864	-0.306	0.573	0.640
11/16	MC-20	2	2.61	2.23	4.65	5.80	-0.31	-0.89	37.65	-0.203	1.980	-8.234	-0.335	0.543	0.609
11/17	MC-17	2	-1.02	-1.36	-2.80	-3.46	0.10	-4.63	33.94	-0.375	-0.078	3.061	-0.296	0.584	0.651
11/17	MC-17	2	-0.47	-1.05	-1.91	-2.79	0.71	-4.06	34.25	-0.348	-0.018	2.489	-0.294	0.587	0.653
11/17	MC-19	2	-0.61	-1.85	-2.87	-4.85	0.72	-4.18	33.42	-0.381	-0.475	4.225	-0.299	0.581	0.647
11/18	MC-17	2	-0.86	-0.60	-1.90	-1.46	0.60	-4.49	34.72	-0.386	0.412	1.891	-0.333	0.545	0.611
11/18	MC-19	2	-0.82	-2.09	-3.31	-5.48	0.48	-4.39	33.18	-0.382	-0.639	4.659	-0.288	0.593	0.660
11/18	MC-13	2	-0.73	-0.75	-1.89	-1.97	0.34	-4.34	34.57	-0.365	0.190	1.784	-0.311	0.568	0.634
11/20	MC-17	2	-0.64	-1.17	-2.22	-2.54	-0.46	-4.23	34.13	-0.364	0.472	1.731	-0.301	0.579	0.645

[a] PPQ correction of Petersen and others (2016) already applied.

TABLE A3

Interval windows and corresponding transfer function values. Brand ^{17}O correction

Run Interval	Equilibrated Gas Line Slope	Empirical Transfer Function Slope	Equilibrated Transfer Function Intercept
May-June 2012			
5/14 -5/23	0.0315	1.0977	0.9811
5/24 - 6/12	0.0315	1.0731	0.9593
October-November 2012			
10/23 -11/12	0.0251	1.0791	0.9407
5/24 - 6/12	0.0283	1.0767	0.9028

TABLE A4

Clumped isotope data - santrock method

Date	Name	Window	δ^{45}	δ^{46}	δ^{47}	δ^{48}	δ^{49}	$\delta^{13}C$	$\delta^{18}O$	Δ_{47}	Δ_{48}	Δ_{49}	$\Delta_{47\text{-SGvWG}}$	$\Delta_{47\text{-RF}}$	$\Delta_{47\text{-RF-AC}}$
May-June 2012															
6/11	MC-14	2	-1.39	-2.04	-3.96	-5.47	-88.69	-5.10	32.87	-0.519	-1.394	-83.657	-0.393	0.600	0.666
6/12	MC-15	2	-1.67	-1.99	-4.20	-5.47	-155.86	-5.40	32.92	-0.520	-1.496	-151.033	-0.387	0.607	0.673
6/12	MC-16	2	-1.49	-1.61	-3.62	-4.39	-152.22	-5.23	33.31	-0.499	-1.169	-148.167	-0.384	0.610	0.677
October-November 2012: Samples and Standards															
10/27	MC-14	1	-1.27	-1.85	-3.56	-4.73	15.17	-4.97	33.07	-0.442	-1.043	20.239	-0.352	0.620	0.687
10/27	MC-15	1	-1.67	-1.89	-4.03	-4.87	8.32	-5.40	33.03	-0.461	-1.103	13.876	-0.360	0.612	0.678
10/27	MC-16	1	-1.29	-1.16	-2.89	-2.93	-24.80	-5.03	33.78	-0.415	-0.609	-21.218	-0.342	0.631	0.697
10/28	MC-14	1	-1.14	-1.80	-3.38	-4.90	6.28	-4.84	33.12	-0.436	-1.302	11.083	-0.351	0.622	0.688
10/28	MC-15	1	-1.55	-1.79	-3.77	-4.54	-29.58	-5.28	33.13	-0.417	-0.977	-24.550	-0.322	0.653	0.719
10/28	MC-16	1	-1.30	-1.17	-2.89	-2.77	-4.25	-5.04	33.77	-0.405	-0.430	-0.569	-0.332	0.642	0.709
10/29	MC-18	1	-1.62	-2.49	-4.56	-6.31	13.35	-5.33	32.40	-0.443	-1.337	20.105	-0.328	0.646	0.712
10/30	MC-13	1	-0.96	-1.12	-2.53	-2.62	4.82	-4.68	33.82	-0.435	-0.390	8.065	-0.371	0.599	0.666
10/30	MC-11	1	-1.72	-1.37	-3.56	-3.54	-16.44	-5.48	33.57	-0.441	-0.811	-11.980	-0.351	0.621	0.688
10/30	MC-15	1	-1.62	-1.89	-3.97	-4.88	-11.93	-5.35	33.03	-0.451	-1.117	-6.544	-0.351	0.621	0.687
10/30	MC-14	1	-1.26	-2.07	-3.79	-5.28	-0.14	-4.96	32.83	-0.456	-1.142	5.298	-0.360	0.611	0.678
10/31	MC-16	1	-1.33	-1.29	-3.07	-3.26	46.27	-5.06	33.65	-0.439	-0.689	50.410	-0.361	0.610	0.677
11/2	MC-18	1	-1.34	-2.30	-4.11	-5.99	-2.61	-5.03	32.60	-0.467	-1.398	3.349	-0.363	0.608	0.674
11/2	MC-13	1	-1.03	-1.40	-2.83	-3.37	-24.42	-4.73	33.53	-0.400	-0.566	-20.661	-0.329	0.645	0.712
11/10	MC-13	2	-0.90	-1.00	-2.35	-2.58	19.10	-4.61	33.94	-0.439	-0.578	22.089	-0.373	0.568	0.635
11/10	MC-18	2	-1.37	-2.35	-4.16	-6.08	9.78	-5.07	32.55	-0.433	-1.388	15.948	-0.315	0.630	0.696
11/11	MC-20	2	2.64	2.39	4.81	6.35	-12.49	-0.96	37.45	-0.266	1.565	-19.863	-0.402	0.536	0.603
11/11	MC-17	2	-0.32	-0.73	-1.47	-2.02	14.45	-4.01	34.22	-0.416	-0.553	16.258	-0.375	0.566	0.632
11/11	MC-11	2	-1.81	-1.60	-3.92	-4.01	-50.25	-5.57	33.33	-0.483	-0.823	-45.417	-0.373	0.568	0.634
11/12	MC-9	2	-1.03	-1.81	-3.27	-4.60	19.02	-4.72	33.11	-0.433	-0.986	23.777	-0.341	0.602	0.669
11/12	MC-20	2	2.78	2.48	5.06	6.95	10.83	-0.81	37.54	-0.257	1.981	2.951	-0.400	0.538	0.605
11/12	MC-11	2	-1.59	-1.21	-3.27	-2.79	41.41	-5.34	33.73	-0.446	-0.376	45.655	-0.354	0.589	0.655
11/12	MC-9	2	-1.02	-1.84	-3.28	-4.81	12.90	-4.71	33.08	-0.426	-1.147	17.665	-0.334	0.610	0.677
11/15	MC-18	2	-1.45	-2.71	-4.66	-6.94	11.52	-5.14	32.17	-0.500	-1.530	18.506	-0.369	0.572	0.639
11/16	MC-9	2	-1.15	-2.05	-3.63	-5.50	29.63	-4.84	32.86	-0.434	-1.415	35.063	-0.331	0.613	0.680

TABLE A4
(continued)

Date	Name	Window	δ^{45}	δ^{46}	δ^{47}	δ^{48}	δ^{49}	$\delta^{13}C$	$\delta^{18}O$	Δ_{47}	Δ_{48}	Δ_{49}	$\Delta_{47\text{-SGvWG}}$	$\Delta_{47\text{-RF}}$	$\Delta_{47\text{-RF-AC}}$
October-November 2012: Samples and Standards															
11/16	MC-11	2	-1.77	-1.31	-3.55	-3.45	31.96	-5.53	33.63	-0.439	-0.829	36.580	-0.339	0.605	0.671
11/16	MC-19	2	-0.68	-1.86	-2.97	-4.94	21.09	-4.35	33.05	-0.433	-1.222	25.587	-0.349	0.594	0.660
11/16	MC-20	2	2.61	2.23	4.65	5.80	12.82	-0.98	37.29	-0.245	1.317	5.588	-0.376	0.564	0.631
11/17	MC-17	2	-1.02	-1.36	-2.80	-3.46	53.94	-4.72	33.58	-0.418	-0.749	57.903	-0.339	0.604	0.671
11/17	MC-17	2	-0.47	-1.05	-1.91	-2.79	26.80	-4.16	33.89	-0.390	-0.689	29.449	-0.336	0.607	0.674
11/17	MC-19	2	-0.61	-1.85	-2.87	-4.85	23.29	-4.27	33.06	-0.423	-1.148	27.703	-0.342	0.601	0.668
11/18	MC-17	2	-0.86	-0.60	-1.90	-1.46	0.90	-4.58	34.36	-0.430	-0.257	3.001	-0.376	0.564	0.631
11/18	MC-19	2	-0.82	-2.09	-3.31	-5.48	64.93	-4.48	32.82	-0.424	-1.312	70.245	-0.330	0.614	0.680
11/18	MC-13	2	-0.73	-0.75	-1.89	-1.97	7.10	-4.44	34.21	-0.408	-0.480	9.359	-0.354	0.588	0.654

TABLE A5

Interval windows and corresponding transfer function values. Santrock method

Run Interval	Equilibrated Gas Line Slope	Empirical Transfer Function Slope	Equilibrated Transfer Function Intercept
May-June 2012			
5/14 -5/23	0.0316	1.1085	1.0453
5/24 - 6/12	0.0316	1.0973	1.0315
October-November 2012			
10/23 -11/12	0.0252	1.0895	1.0035
5/24 - 6/12	0.0282	1.0819	0.9711

REFERENCES

Arguez, A., Durre, I., Applequist, S., Vose, R. S., Squires, M. F., Yin, X., Heim, R. R., and Owen, T. W., 2012, NOAA's 1981–2010 U.S. climate normals-An Overview: Bulletin of the American Meteorological Society, v. 93, p. 1687–1697, https://doi.org/10.1175/BAMS-D-11-00197.1

Barberà, X., Cabrera, L., Marzo, M., Parés, J. M., and Agustí, J., 2001, A complete terrestrial Oligocene magnetobiostratigraphy from the Ebro Basin, Spain: Earth and Planetary Science Letters, v. 187, n. 1–2, p. 1–16, https://doi.org/10.1016/S0012-821X(01)00270-9

Brand, W. A., Assonov, S. S., and Coplen, T. B., 2010, Correction for the ^{17}O interference in $\delta(^{13}C)$ measurements when analyzing CO_2 with stable isotope mass spectrometry (IUPAC Technical Report): Pure and Applied Chemistry, v. 82, n. 8, p. 1719–1733, https://doi.org/10.1351/PAC-REP-09-01-05

Breecker, D. O., Sharp, Z. D., and McFadden, L. D., 2009, Seasonal bias in the formation and stable isotopic composition of pedogenic carbonate in modern soils from central New Mexico, USA: GSA Bulletin, v. 121, n. 3–4, p. 630–640, https://doi.org/10.1130/B26413.1

Breshears, D. D., Nyhan, J. W., Heil, C. E., and Wilcox, B. P., 1998, Effects of Woody Plants on Microclimate in a Semiarid Woodland: Soil Temperature and Evaporation in Canopy and Intercanopy Patches: International Journal of Plant Sciences, v. 159, n. 6, p. 1010–1017, https://doi.org/10.1086/314083

Brooks, P. D., Schmidt, S. K., and Williams, M. W., 1997, Winter production of CO_2 and N_2O from alpine tundra: Environmental controls and relationship to inter-system C and N fluxes: Oecologia, v. 110, n. 3, p. 403–413, https://doi.org/10.1007/PL00008814

Cerling, T. E., 1999, Stable Carbon Isotopes in Paleosol Carbonates, *in* Thiry, M. and Simon-Coincon, R., editors, Palaeoweathering, Palaeosurfaces and Related Continental Deposits: International Association of Sedimentologists Special Publication 27, p. 43–60, https://doi.org/10.1002/9781444304190.ch2

Colwyn, D. A., and Hren, M. T., 2019, An abrupt decrease in Southern Hemisphere terrestrial temperature during the Eocene–Oligocene transition: Earth and Planetary Science Letters, v. 512, p. 227–235, https://doi.org/10.1016/j.epsl.2019.01.052

Costa, E., Garcés, M., Sáez, A., Cabrera, L., and López-Blanco, M., 2011, The age of the "Grande Coupure" mammal turnover: New constraints from the Eocene-Oligocene record of the Eastern Ebro Basin (NE Spain): Palaeogeography, Palaeoclimatology, Palaeoecology, v. 301, n. 1–4, p. 97–107, https://doi.org/10.1016/j.palaeo.2011.01.005

Coxall, H. K., and Wilson, P. A., 2011, Early Oligocene glaciation and productivity in the eastern equatorial Pacific: Insights into global carbon cycling: Paleoceanography, v. 26, n. 2, p. 1–18, https://doi.org/10.1029/2010PA002021

Coxall, H. K., Wilson, P. A., Pälike, H., Lear, C. H., and Backman, J., 2005, Rapid stepwise onset of Antarctic glaciation and deeper calcite compensation in the Pacific Ocean: Nature, v. 433, p. 53–57, https://doi.org/10.1038/nature03135

Cramer, B. S., Toggweiler, J. R., Wright, J. D., Katz, M. E., and Miller, K. G., 2009, Ocean overturning since the Late Cretaceous: Inferences from a new benthic foraminiferal isotope compilation: Paleoceanography, v. 24, n. 4, p. 1–14, https://doi.org/10.1029/2008PA001683

Daëron, M., Blamart, D., Peral, M., and Affek, H. P., 2016, Absolute isotopic abundance ratios and the accuracy of Δ_{47} measurements: Chemical Geology, v. 442, p. 83–96, https://doi.org/10.1016/j.chemgeo.2016.08.014

Decker, K. L. M., Wang, D., Waite, C., and Scherbatskoy, T., 2003, Snow removal and ambient air temperature effects on forest soil temperatures in northern Vermont: Soil Science Society of America Journal, v. 67, n. 4, p. 1234–1243, https://doi.org/10.2136/sssaj2003.1234

Defliese, W. F., Hren, M. T., and Lohmann, K. C., 2015, Compositional and temperature effects of

phosphoric acid fractionation on Δ_{47} analysis and implications for discrepant calibrations: Chemical Geology, v. 396, p. 51–60, https://doi.org/10.1016/j.chemgeo.2014.12.018
Delgado, A., and Reyes, E., 1996, Oxygen and hydrogen isotope compositions in clay minerals: A potential single-mineral geothermometer: Geochimica et Cosmochimica Acta, v. 60, p. 4285–4289, https://doi.org/10.1016/S0016-7037(96)00260-8
Dennis, K. J., Affek, H. P., Passey, B. H., Schrag, D. P., and Eiler, J. M., 2011, Defining an absolute reference frame for "clumped" isotope studies of CO_2: Geochimica et Cosmochimica Acta, v. 75, n. 22, p. 7117–7131, https://doi.org/10.1016/j.gca.2011.09.025
Dworkin, S. I., Nordt, L., and Atchley, S., 2005, Determining terrestrial paleotemperatures using the oxygen isotopic composition of pedogenic carbonate: Earth and Planetary Science Letters, v. 237, n. 1–2, p. 56–68, https://doi.org/10.1016/j.epsl.2005.06.054
Edwards, E. J., Osborne, C. P., Stromberg, C. A. E., Smith, S. A., Bond, W. J., Christin, P. A., Cousins, A. B., Duvall, M. R., Fox, D. L., Freckleton, R. P., Ghannoum, O., Hartwell, J., Huang, Y., Janis, C. M., and others, 2010, The Origins of C_4 Grasslands: Integrating Evolutionary and Ecosystem Science: Science, v. 328, n. 5978, p. 587–591, https://doi.org/10.1126/science.1177216
Eiler, J. M., 2011, Paleoclimate reconstruction using carbonate clumped isotope thermometry: Quaternary Science Reviews, v. 30, n. 25–26, p. 3575–3588, https://doi.org/10.1016/j.quascirev.2011.09.001
Fan, M., Hough, B. G., and Passey, B. H., 2014, Middle to late Cenozoic cooling and high topography in the central Rocky Mountains: Constraints from clumped isotope geochemistry: Earth and Planetary Science Letters, v. 408, p. 35–47, https://doi.org/10.1016/j.epsl.2014.09.050
Fan, M., Ayyash, S. A., Tripati, A., Passey, B. H., and Griffith, E. M., 2017, Terrestrial cooling and changes in hydroclimate in the continental interior of the United States across the Eocene-Oligocene boundary: GSA Bulletin, v. 130, n. 7–8, p. 1073–1084, https://doi.org/10.1130/B31732.1
Fick, S. E., and Hijmans, R. J., 2017, WorldClim 2: New 1-km spatial resolution climate surfaces for global land areas: International Journal of Climatology, v. 37, n. 12, p. 4302–4315, https://doi.org/10.1002/joc.5086
Fuchs, M., Campbell, G. S., and Papendick, R. I., 1978, An Analysis of Sensible and Latent Heat Flow in a Partially Frozen Unsaturated Soil: Soil Science Society of America Journal, v. 42, n. 3, p. 379–385, https://doi.org/10.2136/sssaj1978.03615995004200030001x
Galeotti, S., DeConto, R., Naish, T., Stocchi, P., Florindo, F., Pagani, M., Barrett, P., Bohaty, S. M., Lanci, L., Pollard, D., Sandroni, S., Talarico, F. M., and Zachos, J. C., 2016, Antarctic Ice Sheet variability across the Eocene-Oligocene boundary climate transition: Science, v. 352, n. 6281, p. 76–80, https://doi.org/10.1126/science.aab0669
Gallagher, T. M., and Sheldon, N. D., 2013, A new paleothermometer for forest paleosols and its implications for Cenozoic climate: Geology, v. 41, n. 6, p. 647–650, https://doi.org/10.1130/G34074.1
_____ 2016, Combining soil water balance and clumped isotopes to understand the nature and timing of pedogenic carbonate formation: Chemical Geology, v. 435, p. 79–91, https://doi.org/10.1016/j.chemgeo.2016.04.023
Gallagher, T. M., Sheldon, N. D., Mauk, J. L., Petersen, S. V., Gueneli, N., and Brocks, J. J., 2017, Constraining the thermal history of the North American Midcontinent Rift System using carbonate clumped isotopes and organic thermal maturity indices: Precambrian Research, v. 294, p. 53–66, https://doi.org/10.1016/j.precamres.2017.03.022
Garcés, M., López-Blanco, M., Valero, L., Beamud, E., Oliva, B., Vinyoles, A., Arbués, P., Cabello, P., and Cabrera, L., 2018, Sedimentary trends, shifts and breaks across the South-Pyrenean Foreland Syste: 20th EGU General Assembly, p. 15846.
Garcia-Castellanos, D., Vergés, J., Gaspar-Escribano, J., and Cloetingh, S., 2003, Interplay between tectonics, climate, and fluvial transport during the Cenozoic evolution of the Ebro Basin (NE Iberia): Journal of Geophysical Research-Solid Earth, v. 108, n. B7, p. 1–18, https://doi.org/10.1029/2002JB002073
Garzione, C. N., Auerbach, D. J., Jin-Sook Smith, J., Rosario, J. J., Passey, B. H., Jordan, T. E., and Eiler, J. M., 2014, Clumped isotope evidence for diachronous surface cooling of the Altiplano and pulsed surface uplift of the Central Andes: Earth and Planetary Science Letters, v. 393, p. 173–181, https://doi.org/10.1016/j.epsl.2014.02.029
Geiger, R., Aron, R. H., and Todhunter, P., 1995, The Climate Near the Ground: Braunschweig, Germany, Vieweg, 358 p., https://doi.org/10.1007/978-3-322-86582-3
Ghosh, P., Adkins, J., Affek, H., Balta, B., Guo, W., Schauble, E. A., Schrag, D., and Eiler, J. M., 2006a, ^{13}C–^{18}O bonds in carbonate minerals: A new kind of paleothermometer: Geochimica et Cosmochimica Acta, v. 70, n. 6, p. 1439–1456, https://doi.org/10.1016/j.gca.2005.11.014
Ghosh, P., Garzione, C. N., and Eiler, J. M., 2006b, Rapid Uplift of the Altiplano Revealed Through ^{13}C-^{18}O Bonds in Paleosol Carbonates: Science, v. 311, n. 5760, p. 511–515, https://doi.org/10.1126/science.1119365
Grujic, D., Govin, G., Barrier, L., Bookhagen, B., Coutand, I., Cowan, B., Hren, M. T., and Najman, Y., 2018, Formation of a Rain Shadow: O and H Stable Isotope Records in Authigenic Clays From the Siwalik Group in Eastern Bhutan: Geochemistry, Geophysics, Geosystems, v. 19, n. 9, p. 3430–3447, https://doi.org/10.1029/2017GC007254
Hardy, J. P., Groffman, P. M., Fitzhugh, R. D., Henry, K. S., Welman, A. T., Demers, J. D., Fahey, T. J., Driscoll, C. T., Tierney, G. L., and Nolan, S., 2001, Snow depth manipulation and its influence on soil frost and water dynamics in a northern hardwood forest: Biogeochemistry, v. 56, n. 2, p. 151–174, https://doi.org/10.1023/A:1013036803050
Henkes, G. A., Passey, B. H., Grossman, E. L., Shenton, B. J., Pérez-Huerta, A., and Yancey, T. E., 2014, Temperature limits for preservation of primary calcite clumped isotope paleotemperatures: Geochimica et Cosmochimica Acta, v. 139, p. 362–382, https://doi.org/10.1016/j.gca.2014.04.040
Hentschel, K., Borken, W., Zuber, T., Bogner, C., Huwe, B., and Matzner, E., 2009, Effects of soil frost on

nitrogen net mineralization, soil solution chemistry and seepage losses in a temperate forest soil: Global Change Biology, v. 15, n. 4, p. 825–836, https://doi.org/10.1111/j.1365-2486.2008.01753.x
Hillel, D., 1980, Fundamentals of Soil Physics: New York, Academic Press, 413 p., https://doi.org/10.1016/B978-0-08-091870-9.50006-6
Hough, B. G., Fan, M., and Passey, B. H., 2014, Calibration of the clumped isotope geothermometer in soil carbonate in Wyoming and Nebraska, USA: Implications for paleoelevation and paleoclimate reconstruction: Earth and Planetary Science Letters, v. 391, p. 110–120, https://doi.org/10.1016/j.epsl.2014.01.008
Hren, M. T., Sheldon, N. D., Grimes, S. T., Collinson, M. E., Hooker, J. J., Bugler, M., and Lohmann, K. C., 2013, Terrestrial cooling in Northern Europe during the Eocene-Oligocene transition: Proceedings of the National Academy of Sciences of the United States of America, v. 110, n. 19, p. 7562–7567, https://doi.org/10.1073/pnas.1210930110
Huber, M., and Caballero, R., 2011, The early Eocene equable climate problem revisited: Climate of the Past, v. 7, n. 2, p. 603–633, https://doi.org/10.5194/cp-7-603-2011
Huntington, K. W., Budd, D. A., Wernicke, B. P., and Eiler, J. M., 2011, Use of Clumped-Isotope Thermometry To Constrain the Crystallization Temperature of Diagenetic Calcite: Journal of Sedimentary Research, v. 81, n. 9, p. 656–669, https://doi.org/10.2110/jsr.2011.51
Hyland, E. G., Huntington, K. W., Sheldon, N. D., and Reichgelt, T., 2018, Temperature seasonality in the North American continental interior during the Early Eocene Climatic Optimum: Climate of the Past, v. 14, n. 10, p. 1391–1404, https://doi.org/10.5194/cp-14-1391-2018
Kelson, J. R., Watford, D., Bataille, C., Huntington, K. W., Hyland, E., and Bowen, G. J., 2018, Warm Terrestrial Subtropics During the Paleocene and Eocene: Carbonate Clumped Isotope ($_{\Delta}47$) Evidence From the Tornillo Basin, Texas (USA): Paleoceanography and Paleoclimatology, v. 33, n. 11, p. 1230–1249, https://doi.org/10.1029/2018PA003391
Kluge, T., John, C. M., Jourdan, A. L., Davis, S., and Crawshaw, J., 2015, Laboratory calibration of the calcium carbonate clumped isotope thermometer in the 25-250 °C temperature range: Geochimica et Cosmochimica Acta, v. 157, p. 213–227, https://doi.org/10.1016/j.gca.2015.02.028
Koch, P. L., Clyde, W. C., Hepple, R. P., Fogel, M. L., Wing, S. L., and Zachos, J. C., 2003, Carbon and oxygen isotope records from Paleosols spanning the Paleocene-Eocene boundary, Bighorn Basin, Wyoming, *in* Wing, S., Gingerich, P. D., Schmitz, B., and Thomas, E., editors, Causes and consequences of globally warm climates in the early Paleogene: Geological Society of America Special Paper 369, p. 49–64, https://doi.org/10.1130/0-8137-2369-8.49
Kohn, M. J., Strömberg, C. A. E., Madden, R. H., Dunn, R. E., Evans, S., Palacios, A., and Carlini, A. A., 2015, Quasi-static Eocene-Oligocene climate in Patagonia promotes slow faunal evolution and mid-Cenozoic global cooling: Palaeogeography, Palaeoclimatology, Palaeoecology, v. 435, p. 24–37, https://doi.org/10.1016/j.palaeo.2015.05.028
Lear, C. H., Bailey, T. R., Pearson, P. N., Coxall, H. K., and Rosenthal, Y., 2008, Cooling and ice growth across the Eocene-Oligocene transition: Geology, v. 36, n. 3, p. 251–254, https://doi.org/10.1130/G24584A.1
Liu, Z., Pagani, M., Zinniker, D., Deconto, R. M., Huber, M., Brinkhuis, H., Shah, S. R., Leckie, R. M., and Pearson, A., 2009, Global Cooling During the Eocene-Oligocene Climate Transition: Science, v. 323, n. 5918, p. 1187–1190, https://doi.org/10.1126/science.1166368
Lohmann, K. C., 1988, Geochemical Patterns of Meteoric Diagenetic Systems and Their Application to Studies of Paleokarst, *in* James, N. P., and Choquette, P. W., editors, Paleokarst: New York, Springer-Verlag, p. 58–80, https://doi.org/10.1007/978-1-4612-3748-8[lowen]3
McElwain, J. C., Beerling, D. J., and Woodward, F. I., 1999, Fossil Plants and Global Warming at the Triassic-Jurassic Boundary: Science, v. 285, n. 5432, p. 1386–1390, https://doi.org/10.1126/science.285.5432.1386
NCDC, 2012, U.S. Climate Normals, accessed July 20, 2005, at https://www.ncdc.noaa.gov/data-access/land-based-station-data/land-based-datasets/climate-normals/1981-2010-normals-data.
Nordt, L. C., and Driese, S. D., 2010, New weathering index improves paleorainfall estimates from Vertisols: Geology, v. 38, n. 5, p. 407–410, https://doi.org/10.1130/G30689.1
Nordt, L., Orosz, M., Driese, S., and Tubbs, J., 2006, Vertisol Carbonate Properties in Relation to Mean Annual Precipitation: Implications for Paleoprecipitation Estimates: The Journal of Geology, v. 114, n. 4, p. 501–510, https://doi.org/10.1086/504182
NRCS, 2016, Soil climate analysis network, accessed June 1, 2016, at https://www.wcc.nrcs.usda.gov/scan/.
Oliver, S. A., Oliver, H. R., Wallace, J. S., and Roberts, A. M., 1987, Soil heat flux and temperature variation with vegetation, soil type and climate: Agricultural and Forest Meteorology, v. 39, n. 2–3, p. 257–269, https://doi.org/10.1016/0168-1923(87)90042-6
Óskarsson, B. V., Riishuus, M. S., and Arnalds, Ó., 2012, Climate-dependent chemical weathering of volcanic soils in Iceland: Geoderma, v. 189–190, p. 635–651, https://doi.org/10.1016/j.geoderma.2012.05.030
Passey, B. H., Levin, N. E., Cerling, T. E., Brown, F. H., and Eiler, J. M., 2010, High-temperature environments of human evolution in East Africa based on bond ordering in paleosol carbonates: Proceedings of the National Academy of Sciences of the United States of America, v. 107, p. n. 25, 11245–11249, https://doi.org/10.1073/pnas.1001824107
Pearson, P. N., McMillan, I. K., Wade, B. S., Jones, T. D., Coxall, H. K., Bown, P. R., and Lear, C. H., 2008, Extinction and environmental change across the Eocene-Oligocene boundary in Tanzania: Geology, v. 36, n. 2, p. 179–182, https://doi.org/10.1130/G24308A.1
Pearson, P. N., Foster, G. L., and Wade, B. S., 2009, Atmospheric carbon dioxide through the Eocene-Oligocene climate transition: Nature, v. 461, p. 1110–1113, https://doi.org/10.1038/nature08447
Peppe, D. J., Royer, D. L., Cariglino, B., Oliver, S. Y., Newman, S., Leight, E., Enikolopov, G., Fernandez-Burgos, M., Herrera, F., Adams, J. M., Correa, E., Currano, E. D., Erickson, J. M., Hinojosa, L. F., Hoganson, J. W., Iglesias, A., Jaramillo, C. A., Johnson, K. R., Jordan, G J., Kraft, N. J. B., Lovelock, E. C., Lusk, C. H.,Niinemets, U., Peñuelas, J., Rapson, G., Wing, S. L., and Wright, I. J., 2011, Sensitivity of leaf

size and shape to climate: Global patterns and paleoclimatic applications: New Phytologist, v. 190, n. 3, p. 724–739, https://doi.org/10.1111/j.1469-8137.2010.03615.x
Peters, N. A., Huntington, K. W., and Hoke, G. D., 2013, Hot or not? Impact of seasonally variable soil carbonate formation on paleotemperature and O-isotope records from clumped isotope thermometry: Earth and Planetary Science Letters, v. 361, p. 208–218., https://doi.org/10.1016/j.epsl.2012.10.024
Petersen, S. V., Winkelstern, I. Z., Lohmann, K. C., and Meyer, K. W., 2016, The effects of Porapak™ trap temperature on $\delta^{18}O$, $\delta^{13}C$, and Δ_{47} values in preparing samples for clumped isotope analysis: Rapid Communications in Mass Spectrometry, v. 30, n. 1, p. 199–208, https://doi.org/10.1002/rcm.7438
PRISM Climate Group, O. S. U., 2015, 30-year normals: precipitation at 800 m resolution, 1980–2010, accessed April 1, 2017, at http://prism.oregonstate.edu/normals/
Qashu, H. K., and Zinke, P. J., 1964, The influence of vegetation on soil thermal regime at the San Dimas lysimeters: Soil Science Society of America, Proceedings, v. 28, n. 5, p. 703–706, https://doi.org/10.2136/sssaj1964.03615995002800050035x
Quade, J., Eiler, J., Daëron, M., and Achyuthan, H., 2013, The clumped isotope geothermometer in soil and paleosol carbonate: Geochimica et Cosmochimica Acta, v. 105, p. 92–107, https://doi.org/10.1016/j.gca.2012.11.031
Retallack, G. J., 2007, Cenozoic Paleoclimate on Land in North America: The Journal of Geology, v. 115, n. 3, p. 271–294, https://doi.org/10.1086/512753
Retallack, G. J., Smith, R. M. H., and Ward, P. D., 2003, Vertebrate extinction across Permian–Triassic boundary in Karoo Basin, South Africa: GSA Bulletin, v. 115, n. 9, p. 1133, https://doi.org/10.1130/B25215.1
Royer, D. L., 1999, Depth to pedogenic carbonate horizon as a paleoprecipitation indicator?: Geology, v. 27, n. 12, p. 1123–1126, https://doi.org/10.1130/0091-7613(1999)027<1123:DTPCHA>2.3.CO;2
Sanborn, P. T., Smith, C. A. S., Froese, D. G., Zazula, G. D., and Westgate, J. A., 2006, Full-glacial paleosols in perennially frozen loess sequences, Klondike goldfields, Yukon Territory, Canada: Quaternary Research, v. 66, n. 1, p. 147–157, https://doi.org/10.1016/j.yqres.2006.02.008
Schaefer, G. L., Cosh, M. H., and Jackson, T. J., 2007, The USDA Natural Resources Conservation Service Soil Climate Analysis Network (SCAN): Journal of Atmospheric and Oceanic Technology, v. 24, p. 2073–2077, https://doi.org/10.1175/2007JTECHA930.1
Schauer, A. J., Kelson, J., Saenger, C., and Huntington, K. W., 2016, Choice of ^{17}O correction affects clumped isotope (Δ_{47}) values of CO_2 measured with mass spectrometry: Rapid Communications in Mass Spectrometry, v. 30, n. 24, p. 2607–2616, https://doi.org/10.1002/rcm.7743
Sheldon, N. D., 2018, Using Carbon Isotope Equilibrium to Screen Pedogenic Carbonate Oxygen Isotopes: Implications for Paleoaltimetry and Paleotectonic Studies: Geofluids, v. 2018, p. 1–11, https://doi.org/10.1155/2018/5975801
Sheldon, N. D., and Tabor, N. J., 2009, Quantitative paleoenvironmental and paleoclimatic reconstruction using paleosols: Earth-Science Reviews, v. 95, n. 1–2, p. 1–52, https://doi.org/10.1016/j.earscirev.2009.03.004
Sheldon, N. D., Retallack, G. J., and Tanaka, S., 2002, Geochemical Climofunctions from North American Soils and Application to Paleosols across the Eocene–Oligocene Boundary in Oregon: The Journal of Geology, v. 110, n. 6, p. 687–696, https://doi.org/10.1086/342865
Sheldon, N. D., Costa, E., Cabrera, L., and Garcés, M., 2012, Continental Climatic and Weathering Response to the Eocene-Oligocene Transition: The Journal of Geology, v. 120, n. 2, p. 227–236, https://doi.org/10.1086/663984
Shenton, B. J., Grossman, E. L., Passey, B. H., Henkes, G. A., Becker, T. P., Laya, J. C., Perez-Huerta, A., Becker, S. P., and Lawson, M., 2015, Clumped isotope thermometry in deeply buried sedimentary carbonates: The effects of bond reordering and recrystallization: GSA Bulletin, v. 127, n. 7–8, p. 1036–1051, https://doi.org/10.1130/B31169.1
Shukla, M. K., 2014, Soil Physics: an Introduction: Boca Raton, Florida, CRC Press, 478 p.
Sjostrom, D. J., Hren, M. T., and Chamberlain, C. P., 2004, Oxygen isotope records of goethite from ferricrete deposits indicate regionally varying holocene climate change in the Rocky Mountain region, U.S.A.: Quaternary Research, v. 61, p. 64–71, https://doi.org/10.1016/j.yqres.2003.08.008
Sjostrom, D. J., Hren, M. T., Horton, T. W., Waldbauer, J. R., and Chamberlain, C. P., 2006, Stable isotopic evidence for a pre–late Miocene elevation gradient in the Great Plains–Rocky Mountain region, USA, *in* Willett, S. D., Hovius, N., Brandon, M. T., and Fisher, D. M., editors, Tectonics, Climate, and Landscape Evolution: Geological Society of America Special Paper 398, p. 309–319, https://doi.org/10.1130/2006.2398(19)
Smith, G. D., Newhall, F., Robinson, L. H., and Swanson, D., 1964, Soil-Temperature Regimes: their characteristics and predictability: Soil Conservation Service, U.S. Departament of Agriculture, SCS-TP-144.
Snell, K. E., Thrasher, B. L., Eiler, J. M., Koch, P. L., Sloan, L. C., and Tabor, N. J., 2013, Hot summers in the Bighorn Basin during the early Paleogene: Geology, v. 41, n. 1, p. 55–58, https://doi.org/10.1130/G33567.1
Solomon, D. K., and Cerling, T. E., 1987, The annual carbon dioxide cycle in a montane soil: Observations, modeling, and implications for weathering: Water Resources Research, v. 23, n. 12, p. 2257–2265, https://doi.org/10.1029/WR023i012p02257
Sommerfeld, R. A., Mosier, A. R., and Musselman, R. C., 1993, CO_2, CH_4 and N_20 flux through a Wyoming snowpack and implications for global budgets: Nature, p. 140–142, https://doi.org/10.1038/361140a0
Spicer, R. A., Valdes, P. J., Spicer, T. E. V., Craggs, H. J., Srivastava, G., Mehrotra, R. C., and Yang, J., 2009, New developments in CLAMP: Calibration using global gridded meteorological data: Palaeogeography, Palaeoclimatology, Palaeoecology, v. 283, n. 1–2, p. 91–98, https://doi.org/10.1016/j.palaeo.2009.09.009
Steppuhn, A., Micheels, A., Bruch, A. A., Uhl, D., Utescher, T., and Mosbrugger, V., 2007, The sensitivity of

ECHAM4/ML to a double CO_2 scenario for the Late Miocene and the comparison to terrestrial proxy data: Global and Planetary Change, v. 57, n. 3–4, p. 189–212, https://doi.org/10.1016/j.gloplacha.2006.09.003

Stinchcomb, G. E., Nordt, L. C., Driese, S. G., Lukens, W. E., Williamson, F. C., and Tubbs, J. D., 2016, A data-driven spline model designed to predict paleoclimate using paleosol geochemistry: American Journal of Science, v. 316, n. 8, p. 746–777, https://doi.org/10.2475/08.2016.02

Stolper, D. A., and Eiler, J. M., 2015, The kinetics of solid-state isotope-exchange reactions for clumped isotopes: A study of inorganic calcites and apatites from natural and experimental samples: American Journal of Science, v. 315, n. 5, p. 363–411, https://doi.org/10.2475/05.2015.01

Tabor, N. J., and Montañez, I. P., 2005, Oxygen and hydrogen isotope compositions of Permian pedogenic phyllosilicates: Development of modern surface domain arrays and implications for paleotemperature reconstructions: Palaeogeography, Palaeoclimatology, Palaeoecology, v. 223, n. 1–2, p. 127–146, https://doi.org/10.1016/j.palaeo.2005.04.009

Tabor, N. J., and Myers, T. S., 2015, Paleosols as Indicators of Paleoenvironment and Paleoclimate: Annual Review of Earth and Planetary Sciences, v. 43, p. 333–361, https://doi.org/10.1146/annurev-earth-060614-105355

Van Vliet-Lanoë, B., 1998, Frost and soils: Implications for paleosols, paleoclimates and stratigraphy: Catena, v. 34, n. 1–2, p. 157–183, https://doi.org/10.1016/S0341-8162(98)00087-3

Van Vliet-Lanoë, B., Coutard, J.-P., and Pissart, A., 1984, Structures caused by repeated freezing and thawing in various loamy sediments: A comparison of active, fossil and experimental data: Earth Surface Processes and Landforms, v. 9, n. 6, p. 553–565, https://doi.org/10.1002/esp.3290090609

Van Vliet-Lanoë, B., Fox, C. A., and Gubin, S. V., 2004, Micromorphology of Cryosols, *in* Kimble, J. M., editor, Cryosols: Berlin, Heidelberg, Springer Berlin Heidelberg, p. 365–390, https://doi.org/10.1007/978-3-662-06429-0_18

Waltham, D., Docherty, C., and Taberner, C., 2000, Decoupled flexure in the South Pyrenean Foreland: Journal of Geophysical Research: Solid Earth, v. 105, n. B7, p. 16329–16339, https://doi.org/10.1029/2000JB900064

Wing, S. L., Harrington, G. J., Smith, F. A., Bloch, J. I., Boyer, D. M., and Freeman, K. H., 2005, Transient Floral Change and Rapid Global Warming at the Paleo-Eocene Boundary: Science, v. 310, n. 5750, p. 993–996, https://doi.org/10.1126/science.1116913

Yapp, C. J., 1987, Oxygen and hydrogen isotope variations among goethites (α-FeOOH) and the determination of palotemperatures: Geochimica et Cosmochimica Acta, v. 51, n. 2, p. 355–364, https://doi.org/10.1016/0016-7037(87)90247-X

_____ 2000, Climatic implications of surface domains in arrays of δD and $\delta^{18}O$ from hydroxyl minerals: Goethite as an example: Geochimica et Cosmochimica Acta, v. 64, n. 12, p. 2009–2025, https://doi.org/10.1016/S0016-7037(00)00347-1

Zachos, J. C., Dickens, G. R., and Zeebe, R. E., 2008, An early Cenozoic perspective on greenhouse warming and carbon-cycle dynamics: Nature, v. 451, p. 279–283, https://doi.org/10.1038/nature06588

Zanazzi, A., Kohn, M. J., MacFadden, B. J., and Terry, D. O., 2007, Large temperature drop across the Eocene-Oligocene transition in central North America: Nature, v. 445, p. 639–642, https://doi.org/10.1038/nature05551

Zhang, T., 2005, Influence of seasonal snow cover on the ground thermal regime: an overview: Reviews in Geophysics, v. 43, p. 1–23, https://doi.org/10.1029/2004RG000157